**Title: A potent human monoclonal antibody with pan-neutralizing activities directly dislocates S trimer of SARS-CoV-2 through binding both up and down forms of RBD**

**Authors:** Xiaofei Wang[1,2,3,13], Ao Hu[1,13], Xiangyu Chen[4,5,13], Yixin Zhang[1,13], Fei Yu[1,6,13], Shuai Yue[7], Arong Li[2,3], Junsong Zhang[1,6], Zhiwei Pan[7], Yang Yang[7], Yao Lin[7], Leiqiong Gao[7], Jing Zhou[7], Jing Zhao[8], Fang Li[9,10], Yaling Shi[9], Feng Huang[1,6], Xiaofan Yang[1], Yi Peng[1], Luoyang Tu[1], Huan Zhang[11], Huanying Zheng[11], Jun He[12], Hui Zhang[1], Lifan Xu[7], Qizhao Huang[4], Yongqun Zhu[2,3,*], Kai Deng[1,*], Lilin Ye[7,*]

**Affiliations:**

[1]Institute of Human Virology, Key Laboratory of Tropical Disease Control of Ministry of Education, Zhongshan School of Medicine, Sun Yat-sen University, Guangzhou, Guangdong, China.

[2]Department of Gastroenterology of the Second Affiliated Hospital School of Medicine, and Life Sciences Institute, Zhejiang University, Hangzhou, Zhejiang, China.

[3]The MOE Key Laboratory for Biosystems Homeostasis & Protection and Zhejiang Provincial Key Laboratory of Cancer Molecular Cell Biology, Life Sciences Institute, Zhejiang University, Hangzhou, Zhejiang, China.

[4]School of Laboratory Medicine and Biotechnology, Southern Medical University,

22 Guangzhou, Guangdong, China.

23 [5]Institute of Cancer, Xinqiao Hospital, Third Military Medical University, Chongqing

24 400038, China.

25 [6]Medical Research Center, Guangdong Provincial People's Hospital, Guangdong

26 Academy of Medical Sciences, Guangzhou, Guangdong, China.

27 [7]Institute of Immunology, PLA, Third Military Medical University, Chongqing,

28 China.

29 [8]Biomedical Analysis Center, Third Military Medical University, Chongqing, China.

30 [9]Guangzhou Eighth People's Hospital, Guangzhou Medical University, Guangzhou,

31 Guangdong, China.

32 [10]Guangzhou Women and Children Medical Center, Guangzhou Medical University,

33 Guangzhou, Guangdong, China.

34 [11]Guangdong Provincial Center for Disease Control and Prevention, Guangzhou,

35 Guangdong, China.

36 [12]Center for Cell Lineage and Development, Guangzhou Institutes of Biomedicine

37 and Health, Chinese Academy of Sciences, Guangzhou, Guangdong, China.

38 [13]These authors contributed equally to this work.

39 [*]Correspondence: Yongqun Zhu (zhuyongqun@zju.edu.cn), Kai Deng

40 (dengkai6@mail.sysu.edu.cn) and Lilin Ye (yelilinlcmv@tmmu.edu.cn).

41

**Abstract**

The severe acute respiratory syndrome coronavirus 2 (SARS-CoV-2) has caused a global pandemic of novel corona virus disease (COVID-19). The neutralizing monoclonal antibodies (mAbs) targeting the receptor binding domain (RBD) of SARS-CoV-2 are among the most promising strategies to prevent and treat COVID-19. However, SARS-CoV-2 variants of concern (VOCs) profoundly reduced the efficacies of most of mAbs and vaccines approved for clinical use. Herein, we demonstrated mAb 35B5 efficiently neutralizes both wild-type (WT) SARS-CoV-2 and VOCs, including B.1.617.2 (delta) variant, *in vitro* and *in vivo*. Cryo-electron microscopy (cryo-EM) revealed that 35B5 neutralizes SARS-CoV-2 by targeting a unique epitope that avoids the prevailing mutation sites on RBD identified in circulating VOCs, providing the molecular basis for its pan-neutralizing efficacy. The 35B5-binding epitope could also be exploited for the rational design of a universal SARS-CoV-2 vaccine.

57 **Introduction**

58 As of October 26th, 2021, the novel coronavirus SARS-CoV-2 has resulted in more
59 than 243.24 million cases and 4.94 million fatalities[1]. Though an unprecedentedly
60 large number of vaccines and neutralizing mAbs have been developed to contain
61 COVID-19 in the past year, a major concern is the emergence of more transmissible
62 and/or more immune evasive SARS-CoV-2 VOCs, which are antigenically distinct
63 and become dominant in the COVID-19 prevalence over time[2, 3]. Indeed, the D614G
64 variant became prevalent in the early phase of the pandemic and was associated with
65 higher transmission rate [4]. As the thriving pandemic continued, a rapid accumulation
66 of mutations was observed in SARS-CoV-2 and thus seeded the simultaneous
67 appearance of a plethora of VOCs, which include but not limited to B.1.1.7 (UK;
68 alpha variant)[5], B.1.351 (SA; beta variant)[6], P.1 (Brazil; gamma variant)[7] and
69 B.1.617.2 (India; delta variant)[8].

70 In the RBD of SARS-CoV-2 spike protein, B.1.1.7 harbors a N501Y mutation
71 and thus acquires enhanced binding of RBD to the human receptor ACE2[3, 5]. Along
72 with the N501Y mutation, B.1.351 and P.1 develop additional K417N/T and E484K
73 mutations[6, 7]. Meanwhile, B.1.617.2 carries E484Q/L452R mutations[8]. These
74 mutations contribute to the immune escape of SARS-CoV-2 VOCs against many
75 mAbs[3, 9, 10, 11], including those already approved for clinical use (casirivimab,
76 bamlanivimab, regdanvimab). These mutant VOCs also undermine humoral immune
77 response elicited by the WT SARS-CoV-2 infection or vaccines targeting WT

78 SARS-CoV-2 protein sequence[10, 11, 12, 13, 14, 15]. Thus, highly potent and broadly
79 neutralizing mAbs targeting multiple SARS-CoV-2 VOCs are urgently needed for
80 emergency use and elucidating the underlying neutralizing mechanisms of broadly
81 neutralizing mAbs will also provide important insights into the rational design of
82 universal SARS-CoV-2 vaccines.
83
84 **Results**
85 **Isolation and characteristics of mAbs 35B5 and 32C7**
86 To discover potent broadly neutralizing mAbs against circulating SARS-CoV-2 VOCs,
87 we adapted a pipeline to rapidly isolate and characterize mAbs (Supplementary fig.
88 1a). Given the vigorous SARS-CoV-2-specific memory B cell response in individuals
89 recovering from severe COVID-19 illness[16, 17], cryopreserved PBMCs from these
90 convalescent patients with WT SARS-CoV-2 infection were stained for memory B
91 cell markers (CD19, CD20 and IgG) and avidin-tagged biotinylated SARS-CoV-2
92 RBD antigen bait. As expected, we found SARS-CoV-2 RBD-specific memory B
93 cells only enriched in PBMCs of convalescent COVID-19 patients, but not healthy
94 donors (Supplementary fig. 1b). Each individual of SARS-CoV-2 RBD-specific
95 memory B cells was further sorted to clone heavy and light chain pairs for mAb
96 production. Two mAbs potentially with superior neutralization activity, one
97 VH3-9/VK2-28 mAb named as 35B5, characterized by a heavy chain CDR3 region of
98 23 residues and a light chain CDR3 region of 9 residues and another VH3-30/VK4-1

99 mAb named as 32C7, featured by heavy chain CDR3 of 16 residues and light chain
100 CDR3 of 9 residues (Supplementary fig. 1c, d), were cloned, expressed and analyzed.
101 Real-time association and dissociation of 35B5 and 32C7 binding to the RBD of
102 SARS-CoV-2 virus were monitored using the surface plasmon resonance (SPR)-based
103 optical assay. We found that 35B5 and 32C7 exhibited different binding affinity in
104 binding to SARS-CoV-2 RBD. Notably, 35B5 exhibited fast-on/slow-off kinetics with
105 an equilibrium dissociation constant ($K_D$) of $2.19\times10^{-12}$ M and its binding affinity for
106 SARS-CoV-2 RBD is close to the detection limit at sub-nM level (Fig. 1a); whereas
107 32C7 showed slow-on/fast-off kinetics with a $K_D$ of $1.09\times10^{-8}$ M (Fig. 1b).
108 Consistently, these binding modes were further evidenced by enzyme-linked
109 immunosorbent assay (ELISA) for SARS-CoV-2 RBD, with a $EC_{50}$ value of 0.0183
110 μg/ml for 35B5 and a $EC_{50}$ value of 0.1038 μg/ml for 32C7 (Supplementary fig. 1e).
111
112 **Potent neutralization capacity of mAbs 35B5 to SARS-CoV-2 virus *in vitro* and *in***
113 ***vivo***
114 We next investigated the neutralizing capacity of 35B5 and 32C7 against authentic
115 WT SARS-CoV-2 infection in Vero E6 cells. Remarkably, we found that both 35B5
116 and 32C7 neutralized authentic SARS-CoV-2 virus in the low picomolar range, with
117 observed $IC_{50}$ values of 1.55 ng/ml for 35B5 (Fig. 1c) and 8.60 ng/ml for 32C7 (Fig.
118 1d). We further assessed *in vivo* protection efficacy of 35B5 and 32C7 in the human
119 ACE2 (hACE2)-expressing transgenic mouse model (ICR background) that is

120 sensitized to SARS-CoV-2 infection[18]. The hACE2-humanized mice were treated
121 intraperitoneally with a single dose of 35B5 or 32C7 with 20 mg/kg at 6 hours after
122 intranasal infection with $4\times10^4$ PFU of SARS-CoV-2. As control, infected mice of
123 mock group were administrated with an equal volume of PBS (Fig. 1e). At day 5
124 post-infection, the viral loads in the lungs of the mock group surged to ~$10^4$ RNA
125 copies/ml (Fig. 1f). By contrast, 35B5 and 32C7 treatment remarkably reduced the
126 viral titers, with ~$10^2$ RNA copies/ml resulting 100-fold reduction and ~$10^3$ RNA
127 copies/ml resulting 10-fold reduction, respectively (Fig. 1f). In addition, we also
128 determined whether 35B5 and 32C7 treatment ameliorated the pathological lung
129 damage in the hACE2 mice infected with SARS-CoV-2. The transcripts of cytokines
130 and chemokines (e.g., *Ccl2*, *Cxcl1*, *Il1b*, *Il6* and *Tnf*), indicative of tissue
131 inflammation, were greatly reduced in both 35B5- and 32C7-treated groups when
132 compared to those observed in the mock group (Fig. 1g). Parallelly, the SARS-CoV-2
133 virus caused interstitial pneumonia characterized by inflammatory cell infiltration,
134 alveolar septal thickening and distinctive vascular system injury in the mock group,
135 but not in 35B5 or 32C7 treatment groups; additionally, less pronounced lesions of
136 alveolar epithelial cells or focal hemorrhage were observed in the lung sections from
137 mice that received 35B5 or 32C7 treatment than in those from mice of mock group
138 (Fig. 1h). Thus, these results together indicate the potential therapeutic role for these
139 two mAbs, in particular 35B5, in treating COVID-19.
140

141 **35B5 exhibits ultrapotent and broad neutralization activity to SARS-CoV-2**
142 **VOCs *in vitro* and *in vivo***

143 We then sought to determine the neutralizing capacity of 35B5 and 32C7 mAbs
144 against SARS-CoV-2 variants. Neutralizing activity of these two mAbs was assessed
145 against authentic SARS-CoV-2 viruses, including WT, D614G, B.1.351 and B.1.617.2
146 strains. It turned out 35B5 preserved highly potent neutralizing capacity against the
147 D614G variant ($IC_{50}$=7.29 ng/ml), the B.1.351 variant ($IC_{50}$=13.04 ng/ml) and the
148 B.1.617.2 variant ($IC_{50}$=5.63 ng/ml) (Fig. 2a); however, neutralizing capacity of 32C7
149 against these two variants was severely blunted, with $IC_{50}$ values of 127.60 ng/ml for
150 the D614G variant, 1420.00 ng/ml for the B.1.351 variant and 3442.00 ng/ml for the
151 B.1.617.2 variant (Fig. 2b). In parallel, we also explored the neutralization of
152 authentic virus by 35B5 and 32C7 in a focus forming assay (FFA). Consistently, we
153 found that 35B5 showed potent neutralizing capacity against the WT SARS-CoV-2,
154 the D614G variant, the B.1.351 variant as well as the B.1.617.2 variant (Fig. 2c);
155 whereas 32C7 exhibited a clear reduction in neutralization against the D614G variant,
156 the B.1.351 variant and the B.1.617.2 variant (Fig. 2d). Given the highly broad
157 neutralization activities of 35B5 *in vitro*, we next assessed the *in vivo* protection
158 efficacy of 35B5 against the D614G variant, the B.1.351 variant and the B.1.617.2
159 variant. To this end, a different strain of hACE2-humanized mice (C57BL/6
160 background)[19] were infected with $4\times10^4$ PFU of SARS-CoV-2 D614G or B.1.351 or
161 B.1.617.2 and then treated with a single dose of 35B5 with 30 mg/kg or PBS at 4

162 hours after infection. Viral loads in the lungs of all infected mice were measured at
163 day 5 post-infection (Fig. 2e). Indeed, we found that 35B5 treatment resulted in a
164 ~10-fold, ~100-fold and ~100-fold reduction of viral titers in the lungs of mice
165 infected with D614G, B.1.351 and B.1.617.2, respectively (Fig. 2f). Moreover, tissue
166 inflammation and interstitial pneumonia caused by SARS-CoV-2
167 D614G/B.1.351/B.1.617.2 infection were largely ameliorated in 35B5-treated groups
168 compared to that in mock groups (Fig. 2g-j). Together, these results suggest that 35B5
169 potently neutralizes a variety of SARS-CoV-2 variants as a broadly neutralizing mAb.
170

171 **Complex structure of mAb 35B5 with the spike protein**

172 To investigate the structural basis of the superior and broad neutralizing activity of
173 35B5 against the SARS-CoV-2 variants, we employed cryo-EM approaches to
174 determine the complex structure of the Fab region of 35B5 with the spike protein of
175 SARS-CoV-2. Incubation of 35B5 Fab with the ectodomain of the spike protein
176 S-2P[20], a stabilized spike mutant, severely caused the dissociation of the trimer and
177 disrupted its structure quickly *in vitro* (Supplementary Fig. 2). 35B5 Fab even
178 disrupted the ectodomain trimer structure of the spike S-HexaPro protein (S-6P)[21], a
179 more stable spike variant containing four additional proline substitutions (F817P,
180 A892P, A899P and A942P) from S-2P (Supplementary Fig. 2), suggesting that 35B5
181 harbors the potent dissociation activity toward the spike protein. Nonetheless, a few of
182 the S-6P particles were still found to maintain the triangular architecture[21, 22] after

183 35B5 Fab treatment for 3 min, which thereby allowed us to carry out cryo-EM
184 analyses of the 35B5 Fab-S-6P complex. We successfully determined the structures of
185 the 35B5 Fab-S-6P complex in three conformational states to the resolutions of 3.7 Å,
186 3.4 Å and 3.6 Å, respectively (Supplementary Fig. 3 and Supplementary Table 1).
187 In the 35B5 Fab-S-6P complex structure of State 1, two RBD domains of the S-6P
188 trimer are in the standard "up" conformations[20] and are bound by 35B5 Fabs (Fig. 3a).
189 The other RBD domain is in the "down" conformation[20] as that was found in the
190 Fab-free spike trimers. In the 35B5 Fab-S-6P complex structure of State 2, each of the
191 three RBD domains was in the "up" conformation and bound by a 35B5 Fab (Fig. 3a).
192 In the 35B5 Fab-S-6P complex structure of State 3, although all the three RBD
193 domains were bound by 35B5 Fab, only one RBD domain maintained the "up"
194 conformation. The other two RBD domains were in unprecedented conformations,
195 which we for the first time named as "releasing" conformations (Fig. 3a). Compared
196 to the "up" RBDs, the two "releasing" RBD domains move out by 6.4 Å and 23.0 Å,
197 respectively (Fig. 4f). The two "releasing" RBD domains generated large gaps with
198 the adjacent NTD domains in the S-6P trimers (Fig. 3a), suggesting that the spike
199 protein is undergoing structural dissociation.
200
201 **35B5 targets a unique epitope for pan-neutralizing activity**
202 The interactions of 35B5 Fab with the "up" RBDs are identical to those of 35B5 Fab
203 with the "releasing" RBDs in the three states of the 35B5 Fab-S-6P complex. The

204 interface covers a largely buried area of ~1029 $Å^2$ (Fig. 3b, c). The epitope in RBD
205 for 35B5 is composed of 30 interacting residues including R346, F347, N354, R466,
206 A352, K444, Y449, N450, R466, I468, T470, N481, and F490, which form extensive
207 hydrophilic interactions with 35B5 Fab in the structure (Fig. 3b-f). The corresponding
208 paratope in 35B5 Fab consists of two heavy chain complementarity determining
209 regions (CDRH2 and CDRH3) and the heavy chain frameworks (FRH1 and FRH3).
210 The epitope of 35B5 on RBD is distinct from those of the previously identified 4
211 classes of neutralizing antibodies to RBD[23]. The 35B5 Fab-binding surface on RBD is
212 located at the site opposite to the receptor ACE2-binding surface[23, 24, 25, 26], which is
213 targeted by the class 1 antibodies, suggesting that 35B5 doesn't directly block the
214 receptor recognition for neutralization. Although the epitope of 35B5 Fab involves
215 some regions of the epitopes of the classes 2 and 3 of antibodies (Fig. 4a, b and
216 Supplementary Fig. 4a), the major 35B5-interacting residues, including the
217 SARS-CoV-2 specific residues N354, T470 and N481 (Fig. 3b), which are not
218 conserved in the spike proteins of SARS-CoV and MERS-CoV, are outside of the
219 epitopes of the classes 2 and 3 of antibodies. Therefore, 35B5 targets a distinctive
220 epitope to specifically neutralize SARS-CoV-2.

221 The SARS-CoV-2 VOCs contains several prevailing mutations on RBD,
222 including N501Y (B.1.1.7 (alpha), B.1.351 (beta) and P1 (gamma)), K417N (B.1.351
223 (beta) and P1 (gamma)), L452Q (C.37 (lambda)), L452R (B.1.617.2 (delta),
224 B.1.427/B.1.429 (epsilon), B.1.617.1 (kappa) and B.1.526 (iota)), S477N (B.1.526

225 (iota)), T478K (B.1.617.2 (delta)), E484K (B.1.351 (beta), P1 (gamma), B.1.617.2
226 (delta), B.1.525 (eta), and B.1.526 (iota)) and F490S (C.37 (lambda)) (Fig. 5a).
227 However, in the 35B5 Fab-S-6P complex structures, the residues N501, K417, L452,
228 S477, T478 and F490 are not involved in the 35B5-RBD interactions. Only the
229 residue E484 is located at the edge of the 35B5-RBD interface but not contacted by
230 35B5 Fab (Fig. 4c and Fig. 5b). Substitution of E484 by a lysine residue doesn't
231 generate severe structural collision with 35B5 Fab (Fig. 5c). It has been found that
232 L452R mutation is of significant adaptive value to the B.1.617.2 variant (delta).
233 However, L452 has the distance of more than 4.5 Å and 5.1 Å, respectively, to the
234 residues T69 and Y60 of 35B5 Fab in the 35B5 Fab-S-6P complex structure (Fig. 5e),
235 suggesting that the residue is not contacted by 35B5 Fab. Substitution for L452 by an
236 arginine does not spatially affect the 35B5 Fab-RBD contacts. Instead, the mutation
237 generates direct interactions with the residues Y60 and T69 of 35B5 Fab within 3 Å
238 and likely forms two hydrogen bonds (Fig. 5e), suggesting that this mutation does not
239 affect the binding affinity of 35B5 to RBD. Consistently, 35B5 has the comparable
240 super-potent neutralization efficacy to the B.1.617.2 variant as that to the wild-type
241 virus (Fig. 2). Recently, it was found that the C.37 variant (lambda) contains the
242 mutations L452Q and F490S[27]. However, the mutations L452Q and F490S would not
243 structurally affect the interactions of 35B5 Fab with RBD in the 35B5 Fab-S-6P
244 complex structures (Fig. 5f, g), indicating that 35B5 might also exhibit potent
245 neutralizing efficacy to the C.37 variant. Thus, the unique epitope of 35B5 on RBD

246 subtly avoids the prevailing mutation sites, which provides the molecular basis for the
247 potent pan-neutralizing efficacy of 35B5 to the SARS-CoV-2 VOCs.
248
249 **Neutralization mechanism of mAb 35B5**
250 To investigate the neutralization mechanism of 35B5, we analyzed the "down" RBD
251 domain in the State 1 35B5 Fab-S-6P complex. In the density map of the State 1
252 complex, there were some residual densities closed to the "down" RBD domain. We
253 further carried out local refinements on the "down" RBD. The local refinements
254 generated a 4.8-Å density map and revealed that there is a 35B5 Fab contacting the
255 edge of the epitope on the "down" RBD. The low resolution of the local refinement
256 map suggests that the interaction between the 35B5 Fab and the "down" RBD is
257 highly dynamic (Supplementary Fig. 4b-e). Structural modeling after the local
258 refinements revealed that, in contrast to the neutralizing mAbs BD-368[21, 22] and
259 C002[23] recognizing the epitopes that are fully exposed in both "down" and "up"
260 RBDs, 35B5 Fab utilizes the CDRH regions to interact with the residues E340, T345,
261 R346, F347, R346, K444, Y449 and N450 at the exposed edge of the epitope on the
262 "down" RBD, indicating that this RBD domain is being initially recognized by 35B5
263 (Fig. 4d and Supplementary Fig. 4e and Supplementary Fig. 7a, c). Structural
264 superimposition of the 35B5 Fab-"up" RBD model with the "down" RBD in the 35B5
265 Fab-S-6P complex of State 1 or those in the Fab-free spike trimers[21, 28] reveals that the
266 β-sheet and the linking loop of FRH1 of 35B5 Fab have severe structural clashes with

267 the adjacent NTD domain of the spike protein (Fig. 4e), suggesting that upon the
268 high-affinity binding of 35B5 Fab onto the "down" RBD, the spatial collisions
269 between 35B5 Fab and the NTD domain potentially exert repulsion force onto the
270 NTD domain to induce the conformational conversion of RBD from "down" to "up"
271 conformation. Further outward movement of the "up" RBDs generated the "releasing"
272 conformations in the State 3 35B5 Fab-S-6P complex. Thus, the 35B5 Fab-S-6P
273 complex structures in these three states suggest that neutralization of SARS-CoV-2 by
274 35B5 is likely carried out in four sequential steps (Fig. 4g): 35B5 firstly binds to the
275 exposed edge of the epitope to recognizes the "down" RBDs of the spike protein;
276 subsequently, binding of 35B5 imposes structural clashes on the NTD domain to drive
277 the conformational changes of RBDs from "down" to "up"; next, the unstable "up"
278 conformations of the RBD domains destabilizes the structure of the spike trimer and
279 induces the outward movement and releasing of RBDs; finally, the released RBD
280 domains cause the dissociation of the spike trimer.

281 The SARS-CoV-2 VOCs contains the most prevalent mutation D614G in the
282 spike protein, which enhances infectivity by inducing the wedge of a disordered loop
283 between the SD1/CTD1 and NTD domains within a protomer to prevent premature
284 dissociation of the G614 trimer[29]. The residue D614 is not located in the epitope of
285 35B5 (Fig. 3b), thereby having no effects on its binding to the RBD domain.
286 Moreover, upon binding to the "down" RBD domain, the capability of 35B5 to exert
287 the repulsion force onto the NTD domain can counteract the effects of the D614G

288 mutation on the structural arrangement of the spike protein. Therefore, the unique
289 epitope of 35B5 avoiding the prevailing mutation sites on RBD and the repulsion
290 force of 35B5 exerting onto NTD during initial recognition renders its super-potent
291 pan-neutralizing efficacy to the SARS-CoV-2 VOCs.
292
293 **Cryo-EM structure of mAb 32C7**
294 In contrast to 35B5, mAb 32C7 could not efficiently neutralize the SARS-CoV-2
295 VOCs. We also solved the cryo-EM structure of the Fab region of mAb 32C7
296 (hereafter named as 32C7 Fab) in complex with S-6P at a resolution of 2.8 Å
297 (Supplementary Fig. 5 and Supplementary Table 1). The complex structure only
298 contains one 32C7 Fab molecule, which is bound to a "down" RBD domain in the
299 spike protein (Supplementary Fig. 6a-f). The binding surface of 32C7 Fab on RBD
300 overlaps with the epitopes of the class 3 antibodies (Supplementary Fig. 6c),
301 suggesting that 32C7 belongs to the classic class 3 family of neutralizing antibodies.
302 The 32C7 Fab-RBD interface only covers a buried area of approximately 935 $Å^2$,
303 which is much less than that of 35B5 Fab (Fig. 3c and Supplementary Fig. 6g and
304 Supplementary Fig. 7b, d). The smaller epitope surface on RBD determined the
305 weaker neutralization efficacy of 32C7 as compared to that of 35B5 (Fig. 1). In the
306 S-6P-32C7 Fab complex structure, 32C7 Fab does not structurally clash with the NTD
307 domain. Instead, 32C7 Fab interacts with the glycan moiety on the residue N165 of
308 the NTD domain (Supplementary Fig. 6b). In addition to the D614G mutation, the

309 B.1.351 variant harbors 4 amino acid substitutions and 1 deletion of 3 amino acids,
310 which cause the conformational change of the NTD domain. The conformational
311 changes of the NTD domain potentially weaken the interactions of 32C7 Fab with the
312 glycan moiety of N165, and further affect its epitope recognition of RBD, thereby
313 impairing the neutralizing efficacy of 32C7 Fab against the B.1.351 and other VOCs.
314

315 **Discussion**

316 In this study, we demonstrate 35B5 as a ultrapotent and pan-neutralizing human
317 monoclonal antibody against currently circulating SARS-CoV-2 provided by
318 experimental evidence *in vitro* and *in vivo* as well as structural analysis. By contrast,
319 many mAbs such as casirivimab (REGN10933), bamlanivimab (LY-CoV555),
320 etesevimab (LY-CoV016), regdanvimab (CT-P59), ABBV-2B04 (2B04) and 32C7 in
321 the study partially or entirely lose the neutralizing activity against B.1.351 and
322 B.1.617.2[2, 10, 30, 31]. The mechanisms underlying the picomolar broad neutralization by
323 35B5 at least involve three aspects: 1) broad interface and extensive interactions
324 between 35B5 and RBD endow 35B5 as a potent cross-epitope mAb; 2) proactive
325 dissociation of the spike trimer by structural clashes between 35B5 Fab FRH1 and
326 spike NTD domain; 3) no direct contacts between 35B5 Fab and prevailing mutations
327 of SARS-CoV-2 VOCs.

328 Previous works indicated that the ACE-binding surface is partially exposed on the
329 "down" RBDs in the tight- or loose-closed spike trimer[21, 28]. The epitopes of some

330 neutralizing mAbs are also partially exposed on the "down" RBDs[23, 32, 33, 34, 35]. The
331 35B5 Fab-S-6P complex structures in the three states we determined provide for the
332 first time the direct structural evidence for the possibility that the ACE2 or mAbs can
333 approach the partially exposed surface or epitope residues for initial recognition and
334 fulfil the conformational transformation of RBD. In previously identified
335 RBD-targeted mAbs, almost all class 1 mAbs interact extensively with the residues
336 K417 and N501. Most class 2 and class 3 mAbs contact E484, and most class 3 mAbs
337 interact with L452[3]. 35B5 does not directly bind to these prevailing mutant sites. In
338 contrast to the Class 3 mAb S309[26] and the Class 4 mAb CR3022[36], which target the
339 residues conserved in the spike proteins of SARS-CoV, SARS-CoV-2 and
340 MERS-CoV and therefore have cross-species neutralizing activities, 35B5 is a
341 SARS-CoV-2 specific antibody with super potent pan-neutralizing activities to
342 SARS-CoV-2 VOCs.

343 Protective vaccines are considered as keys to terminate the COVID-19 pandemic.
344 However, accumulating evidence suggests that SARS-CoV-2 VOCs compromise
345 neutralization by antibody responses induced by multiple vaccines[12, 13, 14, 15, 37, 38, 39],
346 including mRNA vaccines (BNT162b2 and mRNA-1273), adenovirus-based vaccines
347 (AZD1222 and JNJ-78436735), a nanoparticle-based vaccine (NVX-CoV2373) and
348 an inactivated protein vaccine (Coronavac), primarily due to RBD mutations. Thus,
349 vaccines aimed at eliciting broadly neutralizing mAbs against SARS-CoV-2 VOCs are
350 urgently needed. In the scenario of coping with diverse HIV-1 variants, an

351 experimental pan-HIV-1 vaccine was designed based on the structurally defined
352 epitope of a HIV-1 neutralizing mAb N123-VRC34.01, which targets a linear peptide
353 of fusion peptide that is across-clade conserved[40, 41]. In our study, cryo-EM structure
354 of neutralizing 35B5 to the SARS-CoV-2 spike revealed an epitope that is composed
355 of 30 residues and conserved among all the currently known SARS-CoV-2 VOCs.
356 Importantly, mAb 35B5 was cloned from SARS-CoV-2 RBD-specific B cells
357 obtained from individuals during their early convalescence, which might endow mAb
358 35B5 with limited somatic hypermutation (SHM). In contrast, a broad neutralizing
359 mAb, ADG-2, was engineered by *in vitro* affinity optimization[42] and the extensive
360 SHM makes ADG-2 epitope challenging as a target for SARS-CoV-2 vaccines. Thus,
361 we propose that the 35B5 epitope might be a valuable target for the rational design of
362 a universal SARS-CoV-2 vaccine, which is presumably essential for the ultimate
363 termination of COVID-19 pandemic in the future.
364

365 **Methods**

366 **Human samples.** The COVID-19 patients enrolled in the study were admitted to
367 Guangzhou Eighth People's Hospital (January to March 2020) and provided written
368 informed consent. Blood samples were collected from patients during their
369 convalescence and the time between symptom onset to sample collection was around
370 20 days. Healthy donors were 2 adult participants in the study. Blood samples were
371 collected in cell preparation tubes with sodium citrate (BD Bioscience). Then,
372 peripheral blood mononuclear cells (PBMCs) were isolated from blood samples using
373 Ficoll (TBD Science), washed with PBS, suspended in cell freezing medium (90%

374 FBS plus 10% DMSO), frozen in freezing chamber at -80 °C, and then transferred to
375 liquid nitrogen. The study received IRB approvals at Guangzhou Eighth People's
376 Hospital (KE202001134).
377
378 **Single-cell sorting, RT-PCR and PCR cloning.** PBMCs were firstly incubated with
379 Human TruStain FcX (Biolegend) at 4 °C for 30 min and then stained with
380 biotin-conjugated SARS-CoV-2 RBD protein (Sino Biological, 40592-V05H) at 4 °C
381 for 20 min. Next, PBMCs were stained with PE-Cy7-conjugated streptavidin
382 (eBioscience), FITC-conjugated anti-CD19 antibody (Biolegend), PE-conjugated
383 anti-CD20 antibody (Biolegend), APC-conjugated anti-human IgG (Fc) (Biolegend),
384 APC-Cy7-conjugated anti-CD3 antibody (Biolegend), APC-Cy7-conjugated
385 anti-CD14 antibody (Biolegend), APC-Cy7-conjugated anti-CD56 antibody
386 (Biolegend) and APC-Cy7-conjugated LIVE/DEAD dye (Life Technologies) at 4 °C
387 for 30 min. All the stainings were performed in PBS containing 5% mouse serum
388 (wt/vol). For cell sorting, the SARS-CoV-2 RBD-specific $IgG^+$ B cells were sorted
389 into 96-well plates, with a single cell and 10 μl catch buffer per well. These plates
390 were stored at -80 °C for further usage. Catch buffer: to 1 ml of RNAase-free water
391 (Tiangen Biotech), add 40 μl Rnasin (NEB) and 50 μl 1.5 M Tris pH 8.8 (Beijing
392 Dingguo Changsheng Biotech).
393 IgG VH and VL genes from B cells were PCR amplified and cloned into vectors
394 as previously described[43, 44]. Briefly, plates containing cell lysate were thawed on ice,
395 added with RT-PCR master mix and IgG VH/VL primers per well and performed with
396 RT-PCR following the one step RT-PCR kit protocol (Takara, RR057A). Then,
397 RT-PCR products were nested PCR-amplified with primers for IgG VH or IgG VL
398 following the HS DNA polymerase kit protocol (Takara, TAK R010). The IgG VH
399 and IgG VL nested PCR products were purified and next cloned into human IgG1
400 heavy chain and light chain expression vectors, respectively.
401

402 **Monoclonal antibody production and purification.** Monoclonal antibodies were
403 produced by using the ExpiCHO™ Expression System (Thermo Fisher). Briefly,
404 ExpiCHO-S™ cells of 200 ml ($6\times10^6$ cells/ml) in 1-L flask were transfected with
405 master mixture containing 200 μg heavy chain plasmid, 200 μg light chain plasmid
406 and 640 μl ExpiFectamine™ CHO reagent. On the day after transfection, cultured
407 cells were added with 1.2 ml ExpiCHO™ enhancer and 48 ml ExpiCHO™ feed. A
408 second volume of ExpiCHO™ feed was added into cultured cells on day 5
409 post-transfection. Supernatants were harvested on day 12 post-transfection for
410 antibody purification using rProtein A Sepharose affinity chromatography (Sigma).
411 **Cells and viruses.** Vero E6 cells were obtained from ATCC and maintained in
412 Dulbecco's Modified Essential Medium (DMEM) supplemented with 10% fetal
413 bovine serum (FBS) (ThermoFisher) and 1% penicillin-streptomycin (ThermoFisher)
414 at 37 °C with 5% $CO_2$. The WT SARS-CoV-2 virus (GDPCC-nCOV01, GISAID:
415 EPI_ISL_403934), the B.1.351 variant (SARS-CoV-2/human/CHN/20SF18530/2020
416 strain; GDPCC-nCOV84, National Genomics Data Center:
417 ACC_GD530_GZ_2020-12-10) and the B.1.617.2 variant (GDPCC 2.00096,
418 sequence has not been published) were obtained from the Guangdong Center for
419 Human Pathogen Culture Collection (GDPCC) at Guangdong Provincial Center for
420 Disease Control and Prevention. The D614G variant
421 (hCoV-19/CHN/SYSU-IHV/2020 strain; GISAID: EPI_ISL_444969) was isolated
422 from the sputum of a female infected individual and propagated in Vero E6 cells.
423
424 **Surface Plasmon Resonance (SPR) assay.** SPR experiments were performed using a
425 Biacore® T100 instrument (GE Healthcare, Uppsala, Sweden). All binding analyses
426 were performed at 25 °C using HBS-EP+ (10 mM HEPES, 150 mM NaCl, 3 mM
427 EDTA, 0.005% Tween-20) as the running buffer. Experiments were executed
428 following the previously described SPR protocol[45]. Briefly, RBD protein was
429 immobilized on the sensor chip CM5-type surface raising a final immobilization level

430 of ~600 Resonance Units (RU). Serial dilutions of 35B5 were injected in
431 concentration from 10 to 0.625 nM. Serial dilutions of 32C7 were injected in
432 concentration from 120 to 7.5 nM. For the competitive binding assays, the first
433 sample flew over the chip at a rate of 20 μl/min for 120 s, then the second sample was
434 injected at the same rate for another 200 s. The response units were recorded at room
435 temperature and analyzed using the same software as mentioned above.
436
437 **ELISA.** The ELISA plates were coated with 50 ng of SARS-CoV-2 RBD protein
438 (Sino Biological, 40592-V08H) in 100 μl PBS per well overnight at 4 $^{o}$C. On the next
439 day, the plates were incubated with blocking buffer (5% FBS + 0.1% Tween 20 in
440 PBS) for 1 hour. Then, serially diluted mAbs in 100 μl blocking buffer were added to
441 each well and incubated for 1 hour. After washing with PBST (PBS + 0.1% Tween 20),
442 the bound antibodies were incubated with HRP-conjugated goat anti-human IgG
443 antibody (Bioss Biotech) for 30 min, followed by washing with PBST and addition of
444 TMB (Beyotime). The ELISA plates were allowed to react for ~5 min and then
445 stopped by 1 M $H_2SO_4$ stop buffer. The optical density (OD) value was determined at
446 450 nm. $EC_{50}$ values were determined by using Prism 6.0 (GraphPad) software after
447 log transformation of the mAb concentration using sigmoidal dose-response nonlinear
448 regression analysis.
449
450 **Neutralization assay.** Infectious SARS-CoV-2 neutralization assay was performed
451 according to previous reports[46]. Vero E6 cells were seeded in a 24-well culture plates
452 at a concentration of $4\times10^4$ cells per well at 37 °C for 24 h. For infection with
453 authentic SARS-CoV-2 at an MOI of 0.005, 200 μl of diluted authentic SARS-CoV-2
454 and 5-fold serially diluted 35B5 or 32C7 (from 5 μg/mL to 0.064 μg/mL) mAbs were
455 mixed in the medium with 2% FBS, and were then added into the Vero E6 cells. The
456 culture supernatant was collected at 48h post-infection for focus forming assay and

457 qRT-PCR. $IC_{50}$ values were determined by nonlinear regression using Prism 6.0
458 (GraphPad).
459
460 **Focus forming assay (FFA).** The virus titer was detected by FFA, which is
461 characterized by its high-throughput as compared to the traditional plaque assay[47].
462 Briefly, Vero E6 cells were seeded in 96-well plates 24h prior to infection. Virus
463 cultures were serially diluted and used to inoculate Vero E6 cells at 37°C for 1 h,
464 followed by changed with fresh medium containing 1.6% carboxymethylcellulose.
465 After 24 hours, Vero E6 cells were fixed with 4% paraformaldehyde and
466 permeabilized with 0.5% Triton X-100. Cells were then incubated with
467 anti-SARS-CoV-2 nucleocapsid protein polyclonal antibody (Sino Biological),
468 followed by an HRP-labeled secondary antibody (Proteintech). The foci were
469 visualized by TrueBlue Peroxidase Substrate (SeraCare Life Science), and counted
470 with an ELISPOT reader.
471
472 **Protection against SARS-CoV-2 in hACE2 mice.** All animal experiments were
473 carried out in strict accordance with the guidelines and regulations of Laboratory
474 Monitoring Committee of Guangdong Province of China and were approved by
475 Ethics Committee of Zhongshan School of Medicine of Sun Yat-sen University on
476 Laboratory Animal Care (SYSU-IACUC-2021-00432). Viral infections were
477 performed in a biosafety level 3 (BSL3) facility in accordance with recommendations
478 for the care and use of laboratory animals. The hACE2 mice of the same sex were
479 randomly assigned to each group. For infection, ICR-hACE2 mice were anesthetized
480 with isoflurane and inoculated intranasally with $4\times10^4$ PFU SARS-CoV-2 virus
481 (GISAID: EPI_ISL_402125). Six hours later, the infected mice received a single dose
482 of 35B5 (20 mg/kg) or 32C7 (20 mg/kg) or vehicle. And the H11-K18-hACE2 mice
483 were intranasally challenged with $4\times10^4$ PFU of three subtypes SARS-CoV-2 virus
484 (D614G, B.1.351 and B.1.617.2) per mouse, respectively. Four hours later, the

485 infected mice received a single dose of 35B5 (30 mg/kg) or vehicle. The lungs were
486 collected at day 5 post-infection for further assays.
487
488 **Measurement of viral burden.** For *in vitro* neutralization assay, RNA of culture
489 supernatant was extracted by using TRIzol reagent (Invitrogen). For *in vivo*
490 neutralization assay, lungs of SARS-CoV-2 infected mice were collected and
491 homogenized with gentle MACS M tubes (Miltenyi Biotec, 130-093-236) in a gentle
492 MACS dissociator (Miltenyi Biotec, 130-093-235). Then, total RNA of homogenized
493 lung tissues was extracted with RNeasy Mini Kit (QIAGEN, 74104) according to the
494 manufacturer's instruction. The extracted RNA was performed with quantitative
495 RT-PCR (qRT-PCR) assay to determine the viral RNA copies by using one-step
496 SARS-CoV-2 RNA detection kit (PCR-Fluorescence Probing) (Da An Gene Co.,
497 DA0931).
498 To generate a standard curve, the SARS-CoV-2 nucleocapsid (N) gene was
499 cloned into a pcDNA3.1 expression plasmid and *in vitro* transcribed to obtain RNAs
500 for standards. Indicated copies of N standards were 10-fold serially diluted and
501 proceeded to qRT-PCR utilizing the same one-step SARS-CoV-2 RNA detection kit to
502 obtain standard curves. The reactions were carried out on a QuantStudio 7 Flex
503 System (Applied Biosystems) according to the manufacturer's instruction under the
504 following reaction conditions: 50 °C for 15 min, 95 °C for 15 min, and 45 cycles of
505 94 °C for 15 s and 55 °C for 45 s. The viral RNA copies of each tissue were calculated
506 into copies per ml and presented as log10 scale. The N specific primers and probes
507 were: N-F (5'- CAGTAGGGGAACTTCTCCTGCT-3'), N-R
508 (5'-CTTTGCTGCTGCTTGACAGA-3') and N-P
509 (5'-FAM-CTGGCAATGGCGGTGATGCTGC-BHQ1-3'). In each qRT-PCR
510 experiment, both positive control and negative control of simulated RNA virus
511 particles were included to monitor the entire experimental process and ensure the
512 reliability of the test results.

513

514 **Quantification of cytokine and chemokine mRNA.** RNA was isolated from lung
515 homogenates as described above. Then, cDNA was synthesized from isolated RNA
516 using HiScript III RT SuperMix for qPCR (Vazyme Biotech). The mRNA expression
517 levels of cytokine and chemokine were determined by using ChamQ Universal SYBR
518 q-PCR Master Mix (Vazyme Biotech) with primers for *IL-6* (forward:
519 CCCCAATTTCCAATGCTCTCC; reverse: CGCACTAGGTTTGCCGAGTA), *IL-1b*
520 (forward: TCGCTCAGGGTCACAAGAA; reverse: GTGCTGCCTAATGTCCCCTT),
521 *Tnfa* (forward: ATGGCTCAGGGTCCAACTCT; reverse:
522 CGAGGCTCCAGTGAATTCGG), Ccl2 (forward: AACTGCATCTGCCCTAAGGT;
523 reverse: AGGCATCACAGTCCGAGTCA) and *Cxcl1* (forward:
524 ACTCAAGAATGGTCGCGAGG; reverse: GTGCCATCAGAGCAGTCTGT). The
525 results were normalized to *Gapdh* levels.

526

527 **Histopathology.** At day 5 post-SARS-CoV-2 infection, hACE2 mice were euthanized,
528 and lungs were collected and fixed in 4% paraformaldehyde buffer. Tissues were
529 embedded with paraffin and sections (3-4 mm) were stained with hematoxylin and
530 eosin (H&E).

531

532 **Production and purification of S-2P and S-6P proteins.** The plasmids encoding the
533 ectodomains of the SARS-CoV-2 S-2P and S-6P mutants were kindly provided by Dr.
534 Junyu Xiao. HEK293F cells were cultured in the SMM 293-TI medium (Sino
535 Biological Inc.) at 37 °C with 8% $CO_2$. The S-2P and S-6P plasmids were transiently
536 transfected into HEK293F cells using 25-kDa linear polyethyleneimine (PEI)
537 (Polysciences) with the PEI:DNA mass ratio of 3:1 and 1 mg DNA for per liter of
538 culture when the cell density reached $2 \times 10^6$ cells per mL. At day 4 post-transfection,
539 the supernatants of the cell culture were harvested by centrifugation at 10,000 × g for
540 30 min. The secreted S-2P and S-6P proteins were purified using HisPur$^{TM}$ cobalt

541 resins (Thermo Scientific) and StrepTactin resins (IBA). Further purification was
542 carried out using size-exclusion chromatography with a Superose 6 10/300 column
543 (GE Healthcare) in the buffer containing 20 mM HEPES pH 7.2, 150 mM NaCl and
544 10% Trehalose. The Fab regions of the 35B5 and 32C7 were obtained after the
545 digestion by papain for 40 min at 37 °C in a buffer containing 20 mM HEPES pH 7.2,
546 150 mM NaCl, 5 mM EDTA and 5 mM L-cysteine. The obtained Fabs were purified
547 with a Desalting column (GE Healthcare Life Sciences) to remove L-cysteine, and
548 then further purified in a HiTrap Q column (GE Healthcare Life Sciences). The
549 purified Fabs were collected and concentrated to 0.6 mg/mL.
550
551 **Negative staining analysis.** For negative-staining assays, the S-2P, S-6P, 35B5 Fab
552 and 32C7 Fab proteins were diluted to 0.02 mg/ml in the buffer of 20 mM HEPES,
553 pH 7.2, and 150 mM NaCl. 2 μL of 35B5 Fab or 32C7 Fab was mixed with 2 μL S-2P
554 or S-6P and incubated on ice for 3 and 10 min, respectively, or at room temperature
555 for 30 min. The samples were loaded in the glow-discharged carbon-coated copper
556 grids and stained with 3% Uranyl Acetate (UA). The prepared grids were examined
557 using a Tecnai G2 Spirit BioTWIN transmission electron microscope (FEI) operated
558 at 120 kV. Micrographs were recorded and analyzed using Digital Micrograph
559 software with 120,000× nominal magnification.
560
561 **Cryo-EM sample preparation and data collection.** 2 μL of S-6P (1.2 mg/mL) and 2
562 μL of 35B5 Fab or 32C7 Fab (0.6 mg/mL) were incubated for 3 min at room
563 temperature and then loaded onto the glow-discharged holy-carbon gold grids
564 (Quantifoil, R1.2/1.3). The grids were washed using the buffer containing 20 mM
565 HEPES, pH 7.2, and 150 mM NaCl. The washed grids were blotted using a Mark IV
566 Vitrobot (Thermo Fisher) at 100% humidity and 16 °C for 3 s, and *submerged in*
567 *liquid ethane by plunge-freezing.* For the S-6P-35B5 Fab complex, micrographs were
568 recorded on a FEI Titan Krios (Thermo Fisher) electron microscope operated at 300

569 kV. Totally, 3740 movies were recorded on a K3 Summit direct electron detector
570 (Gatan) in the super-resolution mode (0.5475 Å/pixel) at a nominal magnification of
571 81,000 using a defocus range of 1.2 to 1.3 μm. A GIF Quantum energy filter (Gatan)
572 with a slit width of 20 eV was used on the detector. The micrographs were
573 dose-fractioned into 32 frames with a total electron exposure of ~50 electrons per $Å^2$.
574 For the S-6P-32C7 Fab complex, micrographs were collected on a FEI Titan Krios
575 (Thermo Fisher) operating at 300 kV using the AutoEMation software [48]. Totally,
576 2528 movies were recorded on a K3 Summit direct electron detector (Gatan) in the
577 super-resolution mode (0.53865 Å/pixel) at a nominal magnification of 81,000 using a
578 defocus range of 1.4 to 1.8 μm. A GIF Quantum energy filter (Gatan) with a slit width
579 of 20 eV was used on the detector. The micrographs were dose-fractioned into 32
580 frames with a total electron exposure of ~50 electrons per $Å^2$.
581
582 **Cryo-EM image processing.** Raw movie frames were binned, aligned and averaged
583 into motion-corrected summed images using MotionCor2[49]. The dose-weighted
584 images were then imported into cryoSPARC[50] for the following image processing,
585 including CTF estimation, particle picking and extraction, 2D classification, *ab initio*
586 3D reconstruction, heterogeneous 3D refinement and non-uniform homogeneous
587 refinement. For the S-6P-35B5 Fab complex, 8 representative particle templates were
588 generated in 2D classification of 65,242 particles auto-picked by the blob picker from
589 the first 1000 micrographs. Using these templates, 1,178,527 particles were extracted
590 with a box size of 330×330 and classified into 150 classes in 2D classification.
591 Among them, 43 classes that included 818,470 particles were selected for *ab initio* 3D
592 reconstruction and heterogeneous refinement. Finally, 392,378 particles reconstructed
593 an apparent architecture of the S-6p-35B5 Fab complex and were subjected to two
594 more rounds of *ab initio* 3D reconstruction and heterogeneous refinement before
595 non-uniform refinement. Then the particles were subjected to global and local CTF
596 refinement for final non-uniform refinement, and generated three abundant

597 populations of the S-6P-35B5 Fab complex and structures. Local refinements of the
598 RBD-35B5 Fab region were performed to improve the interface density in
599 *cryoSPARC*. Sharpened maps were generated and validated for model building and
600 refinement. Reported resolutions are based on the gold-standard Fourier shell
601 correlation[51, 52] of 0.143 criterion.

602 For the S-6P-32C7 Fab complex, 4 representative particle templates were
603 generated in 2D classification of 122,851 particles auto-picked by the blob picker
604 from the first 1000 micrographs. Based on these templates, 744,865 particles were
605 extracted with a box size of 380×380 and classified into 150 2D classes. Among them,
606 28 classes including 338,454 particles were selected for *ab initio* 3D reconstruction
607 and heterogeneous refinement. 125,858 particles that reconstructed an apparent
608 architecture of the S-6P-32C7 Fab complex were subjected to two more rounds of *ab*
609 *initio* 3D reconstruction and heterogeneous refinement before non-uniform refinement.
610 Finally, the S-6P-32C7 Fab complex structure that only includes a bound 32C7 Fab
611 was reconstructed from 119,062 particles. Local refinement of the RBD-32C7 Fab
612 region was also performed.

613

614 **Cryo-EM structure modeling and analysis.** To build the S-6P-35B5 Fab complex
615 structural model, an "up" RBD-35B5 Fab model were first generated using a Fab
616 structure (PDB ID: 2X7L) and a RBD model from the Spike trimer (PDB ID: 7K8Y)
617 and manually built in Coot[53] in the locally refined map. The obtained RBD-35B5 Fab
618 model was superimposed with the intact Spike trimer structure (PDB ID: 7K8Y) to
619 generate an initial model of the S-6P-35B5 Fab complex model. The "down"
620 RBD-35B5 Fab model was obtained from fitting the structures of 35B5 Fab, the RBD
621 and NTD domains into the locally refined map of the the S-6P-35B5 Fab complex of
622 State 1 and then validated by *Phenix*[54]. The model building of the S-6P-32C7 Fab
623 complex was carried out in the similar procedure as that of the S-6P-35B5 Fab
624 complex with a Spike trimer structure (PDB ID: 6XKL) as a template. All model

625 building were performed in Coot[53]. Structural refinement and validation were carried
626 out in *Phenix*[54]. Structural figures were generated using UCSF ChimeraX version
627 1.2[55].
628
629 **Statistics.** In the mouse study assessing mAb protection against WT SARS-CoV-2,
630 the comparisons of lung viral titers and lung cytokine/chemokine mRNA were
631 performed using one-way ANOVA with Tukey's post hoc test by Prism 6.0
632 (GraphPad). In the mouse study assessing mAb protection against SARS-CoV-2
633 VOCs, the comparison of lung viral titers was performed using t test (unpaired) by
634 Prism 6.0 (GraphPad).
635
636 **Data and materials availability.** The cryo-EM maps and atomic coordinates have
637 been deposited to the Electron Microscopy Data Bank (EMDB) and Protein Data
638 Bank (PDB) with accession codes EMD-31033 and PDB 7E9N (State 1 of the 35B5
639 Fab-S-6P complex), EMD-31444 and PDB 7F46 ("down" RBD/35B5 Fab local
640 refinement of State 1), EMD-31034 and PDB 7E9O (State 2 of the 35B5 Fab-S-6P
641 complex), EMD-31035 and PDB 7E9P ("up" RBD/35B5 Fab local refinement of
642 State 2), EMD-31036 and PDB 7E9Q (State 3 of the 35B5 Fab-S-6P complex),
643 EMD-31209 and PDB 7ENF (the 32C7 Fab-S-6P complex), and EMD-31210 and
644 PDB 7ENG ("down" RBD/32C7 Fab local refinement).
645
646 **References**

647 1. World Health Organization. Weekly epidemiological update on COVID-19 -
648 26 October 2021.
649 https://www.who.int/publications/m/item/weekly-epidemiological-update-on-c
650 ovid-19---26-october-2021.
651
652 2. Corti D, Purcell LA, Snell G, Veesler D. Tackling COVID-19 with
653 neutralizing monoclonal antibodies. *Cell*.
654
655 3. Yuan M, *et al.* Structural and functional ramifications of antigenic drift in
656 recent SARS-CoV-2 variants. *Science (New York, NY)*, (2021).
657
658 4. Volz E, *et al.* Evaluating the Effects of SARS-CoV-2 Spike Mutation D614G
659 on Transmissibility and Pathogenicity. *Cell* **184**, 64-75.e11 (2021).
660
661 5. Davies NG, *et al.* Estimated transmissibility and impact of SARS-CoV-2
662 lineage B.1.1.7 in England. *Science (New York, NY)* **372**, (2021).
663
664 6. Tegally H, *et al.* Detection of a SARS-CoV-2 variant of concern in South
665 Africa. *Nature* **592**, 438-443 (2021).
666
667 7. Faria NR, *et al.* Genomics and epidemiology of the P.1 SARS-CoV-2 lineage

668 in Manaus, Brazil. *Science (New York, NY)* **372**, 815-821 (2021).

669

670 8. Cherian S*, et al.* Convergent evolution of SARS-CoV-2 spike mutations,
671 L452R, E484Q and P681R, in the second wave of COVID-19 in Maharashtra,
672 India. *bioRxiv : the preprint server for biology*, (2021).

673

674 9. Chen RE*, et al.* Resistance of SARS-CoV-2 variants to neutralization by
675 monoclonal and serum-derived polyclonal antibodies. *Nature medicine*,
676 (2021).

677

678 10. Hoffmann M*, et al.* SARS-CoV-2 variants B.1.351 and P.1 escape from
679 neutralizing antibodies. *Cell*, (2021).

680

681 11. Hoffmann M*, et al.* SARS-CoV-2 variant B.1.617 is resistant to Bamlanivimab
682 and evades antibodies induced by infection and vaccination. *bioRxiv : the*
683 *preprint server for biology*, (2021).

684

685 12. Garcia-Beltran WF*, et al.* Multiple SARS-CoV-2 variants escape
686 neutralization by vaccine-induced humoral immunity. *Cell* **184**,
687 2372-2383.e2379 (2021).

688

689 13. Edara VV, *et al.* Infection- and vaccine-induced antibody binding and
690 neutralization of the B.1.351 SARS-CoV-2 variant. *Cell host & microbe* **29**,
691 516-521.e513 (2021).
692
693 14. Wu K, *et al.* Serum Neutralizing Activity Elicited by mRNA-1273 Vaccine.
694 *The New England journal of medicine* **384**, 1468-1470 (2021).
695
696 15. Wang Z, *et al.* mRNA vaccine-elicited antibodies to SARS-CoV-2 and
697 circulating variants. *Nature*, (2021).
698
699 16. Chen X, *et al.* Disease severity dictates SARS-CoV-2-specific neutralizing
700 antibody responses in COVID-19. *Signal transduction and targeted therapy* **5**,
701 180 (2020).
702
703 17. Sokal A, *et al.* Maturation and persistence of the anti-SARS-CoV-2 memory B
704 cell response. *Cell*, (2021).
705
706 18. Bao L, *et al.* The pathogenicity of SARS-CoV-2 in hACE2 transgenic mice.
707 *Nature* **583**, 830-833 (2020).
708
709 19. Sun SH, *et al.* A Mouse Model of SARS-CoV-2 Infection and Pathogenesis.

710 *Cell host & microbe* **28**, 124-133.e124 (2020).

711

712 20. Wrapp D*, et al.* Cryo-EM structure of the 2019-nCoV spike in the prefusion

713 conformation. *Science (New York, NY)* **367**, 1260-1263 (2020).

714

715 21. Hsieh CL*, et al.* Structure-based design of prefusion-stabilized SARS-CoV-2

716 spikes. *Science (New York, NY)* **369**, 1501-1505 (2020).

717

718 22. Du S*, et al.* Structurally Resolved SARS-CoV-2 Antibody Shows High

719 Efficacy in Severely Infected Hamsters and Provides a Potent Cocktail Pairing

720 Strategy. *Cell* **183**, 1013-1023 e1013 (2020).

721

722 23. Barnes CO*, et al.* SARS-CoV-2 neutralizing antibody structures inform

723 therapeutic strategies. *Nature* **588**, 682-687 (2020).

724

725 24. Benton DJ*, et al.* Receptor binding and priming of the spike protein of

726 SARS-CoV-2 for membrane fusion. *Nature* **588**, 327-330 (2020).

727

728 25. Lan J*, et al.* Structure of the SARS-CoV-2 spike receptor-binding domain

729 bound to the ACE2 receptor. *Nature* **581**, 215-220 (2020).

730

731 26. Pinto D*, et al.* Cross-neutralization of SARS-CoV-2 by a human monoclonal
732 SARS-CoV antibody. *Nature* **583**, 290-295 (2020).
733
734 27. Romero PE*, et al.* The Emergence of SARS-CoV-2 Variant Lambda (C.37) in
735 South America. *medRxiv : the preprint server for health sciences*, (2021).
736
737 28. Toelzer C*, et al.* Free fatty acid binding pocket in the locked structure of
738 SARS-CoV-2 spike protein. *Science (New York, NY)* **370**, 725-730 (2020).
739
740 29. Zhang J*, et al.* Structural impact on SARS-CoV-2 spike protein by D614G
741 substitution. *Science (New York, NY)* **372**, 525-530 (2021).
742
743 30. Dejnirattisai W*, et al.* Antibody evasion by the P.1 strain of SARS-CoV-2. *Cell*
744 **184**, 2939-2954.e2939 (2021).
745
746 31. Wang P*, et al.* Increased resistance of SARS-CoV-2 variant P.1 to antibody
747 neutralization. *Cell host & microbe* **29**, 747-751.e744 (2021).
748
749 32. Lv Z*, et al.* Structural basis for neutralization of SARS-CoV-2 and SARS-CoV
750 by a potent therapeutic antibody. *Science (New York, NY)* **369**, 1505-1509
751 (2020).

752

753 33. Tortorici MA, *et al.* Ultrapotent human antibodies protect against
754 SARS-CoV-2 challenge via multiple mechanisms. *Science (New York, NY)* **370**,
755 950-957 (2020).
756

757 34. Huo J, *et al.* Neutralization of SARS-CoV-2 by Destruction of the Prefusion
758 Spike. *Cell host & microbe* **28**, 497 (2020).
759

760 35. Asarnow D, *et al.* Structural insight into SARS-CoV-2 neutralizing antibodies
761 and modulation of syncytia. *Cell* **184**, 3192-3204 e3116 (2021).
762

763 36. Yuan M, *et al.* A highly conserved cryptic epitope in the receptor binding
764 domains of SARS-CoV-2 and SARS-CoV. *Science (New York, NY)* **368**,
765 630-633 (2020).
766

767 37. Cohen J. South Africa Suspends Use of AstraZeneca's COVID-19 Vaccine
768 after It Fails to Clearly Stop Virus Variant. Science Magazine, February 7,
769 2021.
770 https://www.sciencemag.org/news/2021/02/south-africa-suspendsuse-astrazen
771 ecas-covid-19-vaccine-after-it-fails-clearly-stop., (2021).
772

773 38. Wang GL, *et al.* Susceptibility of Circulating SARS-CoV-2 Variants to
774 Neutralization. *The New England journal of medicine*, (2021).
775
776 39. Herper M, Branswell, H. New Data Shed Light on Efficacy of J&J's
777 Single-Dose Covid Vaccine. Stat, February 24, 2021. https://www.statnews/.
778 com/2021/02/24/new-data-shed-light-on-efficacy-of-jjs-single-dose-vaccineag
779 ainst-covid-19/. (2021).
780
781 40. Xu K, *et al.* Epitope-based vaccine design yields fusion peptide-directed
782 antibodies that neutralize diverse strains of HIV-1. *Nature medicine* **24**,
783 857-867 (2018).
784
785 41. Kong R, *et al.* Fusion peptide of HIV-1 as a site of vulnerability to neutralizing
786 antibody. *Science (New York, NY)* **352**, 828-833 (2016).
787
788 42. Rappazzo CG, *et al.* Broad and potent activity against SARS-like viruses by
789 an engineered human monoclonal antibody. *Science (New York, NY)* **371**,
790 823-829 (2021).
791
792 43. Chen X, *et al.* Human monoclonal antibodies block the binding of
793 SARS-CoV-2 spike protein to angiotensin converting enzyme 2 receptor.

794 *Cellular & molecular immunology* **17**, 647-649 (2020).

795

796 44. Smith K*, et al.* Rapid generation of fully human monoclonal antibodies

797 specific to a vaccinating antigen. *Nature protocols* **4**, 372-384 (2009).

798

799 45. Real-Fernández F*, et al.* Surface plasmon resonance-based methodology for

800 anti-adalimumab antibody identification and kinetic characterization.

801 *Analytical and bioanalytical chemistry* **407**, 7477-7485 (2015).

802

803 46. Ju B*, et al.* Human neutralizing antibodies elicited by SARS-CoV-2 infection.

804 *Nature* **584**, 115-119 (2020).

805

806 47. Sun J*, et al.* Generation of a Broadly Useful Model for COVID-19

807 Pathogenesis, Vaccination, and Treatment. *Cell* **182**, 734-743.e735 (2020).

808

809 48. Lei J, Frank J. Automated acquisition of cryo-electron micrographs for single

810 particle reconstruction on an FEI Tecnai electron microscope. *J Struct Biol*

811 **150**, 69-80 (2005).

812

813 49. Zheng SQ, Palovcak E, Armache JP, Verba KA, Cheng Y, Agard DA.

814 MotionCor2: anisotropic correction of beam-induced motion for improved

815 cryo-electron microscopy. *Nat Methods* **14**, 331-332 (2017).

816

817 50. Punjani A, Rubinstein JL, Fleet DJ, Brubaker MA. cryoSPARC: algorithms for
818 rapid unsupervised cryo-EM structure determination. *Nat Methods* **14**,
819 290-296 (2017).

820

821 51. Henderson R*, et al.* Outcome of the first electron microscopy validation task
822 force meeting. *Structure* **20**, 205-214 (2012).

823

824 52. Scheres SH, Chen S. Prevention of overfitting in cryo-EM structure
825 determination. *Nat Methods* **9**, 853-854 (2012).

826

827 53. Emsley P, Lohkamp B, Scott WG, Cowtan K. Features and development of
828 Coot. *Acta Crystallogr D Biol Crystallogr* **66**, 486-501 (2010).

829

830 54. Liebschner D*, et al.* Macromolecular structure determination using X-rays,
831 neutrons and electrons: recent developments in Phenix. *Acta Crystallogr D*
832 *Struct Biol* **75**, 861-877 (2019).

833

834 55. Pettersen EF*, et al.* UCSF ChimeraX: Structure visualization for researchers,
835 educators, and developers. *Protein science : a publication of the Protein*

*Society* **30**, 70-82 (2021).

**Acknowledgements:** We thank Guangdong Center for Human Pathogen Culture Collection (GDPCC) for providing SARS-CoV-2 isolates. We thank Dr. Junyu Xiao (Peking University) for providing the plasmids encoding the ectodomains of the SARS-CoV-2 S-2P and S-6P mutants. This work was supported by grants from the National Natural Science Fund for Distinguished Young Scholars (No. 31825011 to L.Y.), the National Science and Technology Major Project (No. 2017ZX10202102-006-002 to L.Y.), Guangdong Innovative and Entrepreneurial Research Team Program (2016ZT06S638 to K.D.), High-level Biosafety Laboratory Construction and Operation Program of the Science and Technology Projects of Guangdong Province of China to K.D., the National Natural Science Fund (81925024 to Y. Z.), the National Key Research and Development Program of China (2017YFA0503900 to Y. Z.), and the Fundamental Research Funds for the Central Universities to Y. Z..

**Author contributions:** X.C., S.Y., Z.P., Y.Y., Y.L., J.Z., L.G., J.Z., L.X. and Q.H. collected the PBMC, isolated SARS-CoV-2 RBD-specific B cells and cloned the antibodies; A.H., Y.Z., F.Y., J.Z., F.L., Y.S., F.H., X.Y., Y.P., L.T., H.Z., H.Z., J.H. and H.Z. performed *in vitro* and *in vivo* SARS-CoV-2 virus neutralization assays; X.W. and A.L. performed negative stainings and cryo-EM analyses. L.Y. designed the study and analyzed the data with Y.Z., K.D., X.C., X.W. and A.H.; X.C. wrote the first draft

858 of the manuscript, which was edited by Y.Z., L.Y., K.D., X.W. and A.H.; Y.Z., K.D.

859 and L.Y. supervised the study.

860

861 **Competing interests:** The pending patents of 35B5 and 32C7 have been licensed.

862

863 **Figure 1**

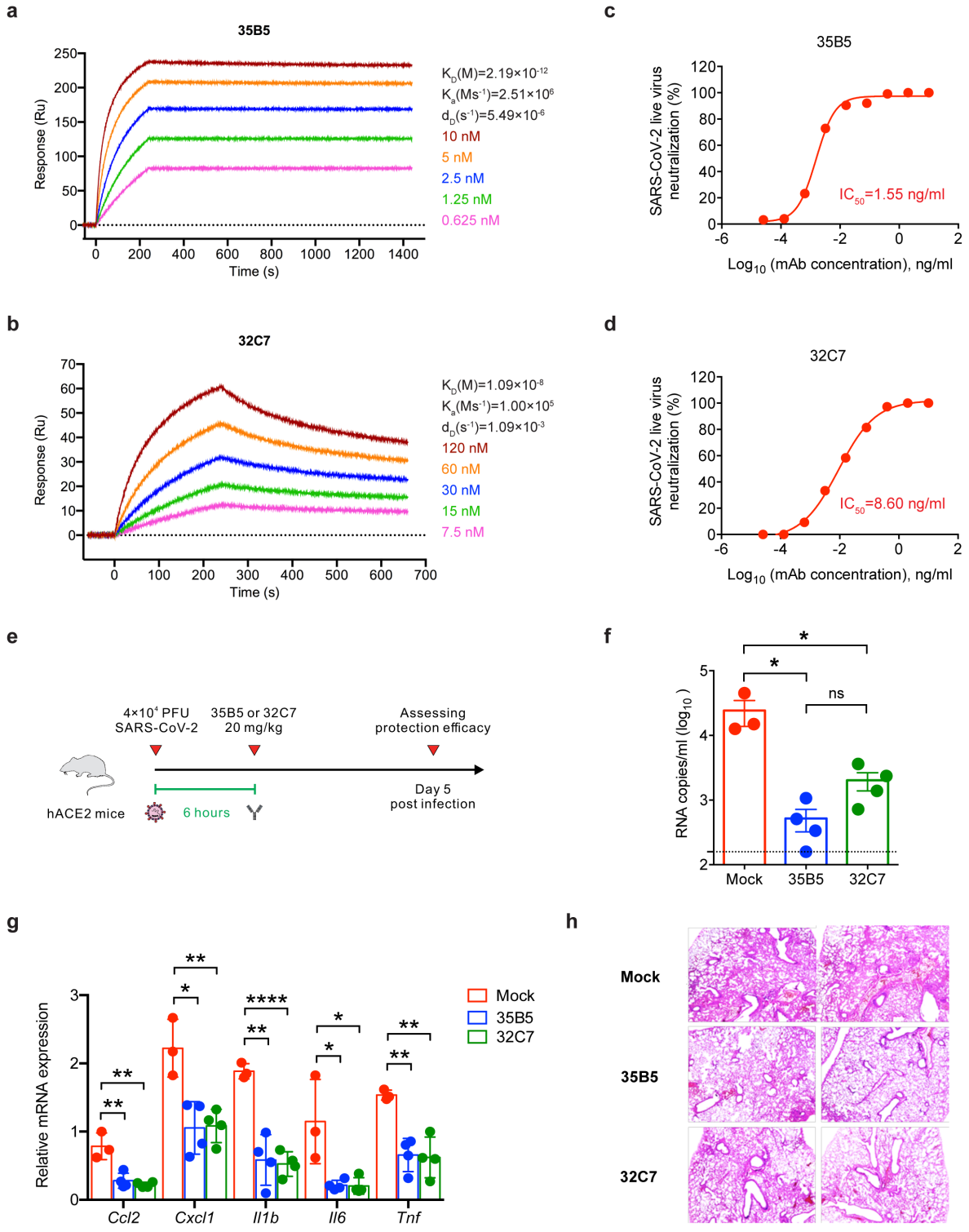


864

865

866 **Fig. 1 35B5 and 32C7 protect against authentic SARS-CoV-2 virus. a**, **b** Affinity
867 analysis of 35B5 (**a**) and 32C7 (**b**) binding to immobilized SARS-CoV-2 RBD by
868 using biolayer interferometry. **c, d** *In vitro* neutralizing activity of 35B5 (**c**) and 32C7
869 (**d**) against authentic SARS-CoV-2. Mixture of SARS-CoV-2 and serially diluted
870 35B5 or 32C7 were added to Vero E6 cells. After 48 hours, $IC_{50}$ values were
871 calculated by fitting the viral RNA copies from serially diluted mAb to a sigmoidal
872 dose-response curve. **e** Schematic diagram of 35B5 and 32C7 treatment *in vivo*. Six
873 hours after infection with $4\times10^4$ PFU SARS-CoV-2, the hACE2 mice received a
874 single dose of 35B5 or 32C7 with 20 mg/kg or no mAb treatment (mock). At day 5
875 post infection, lung tissues were collected for viral burden assessment,
876 cytokine/chemokine assay and histological analysis. **f** Viral titers in the lungs were
877 measured by qRT-PCR and presented as RNA copies per milliliter of lung abrasive
878 fluid. **g** Gene expressions of cytokines and chemokines in the lungs were determined
879 by qPT-PCR. **h** Histopathological analysis of lung tissues. The data are representative
880 of at least two independent experiments. $^*P < 0.05$, $^{**}P < 0.01$ and $^{****}P < 0.0001$.
881 Not significant, ns. Error bars in (**f**) and (**g**) indicate SD.
882

883 **Figure 2**

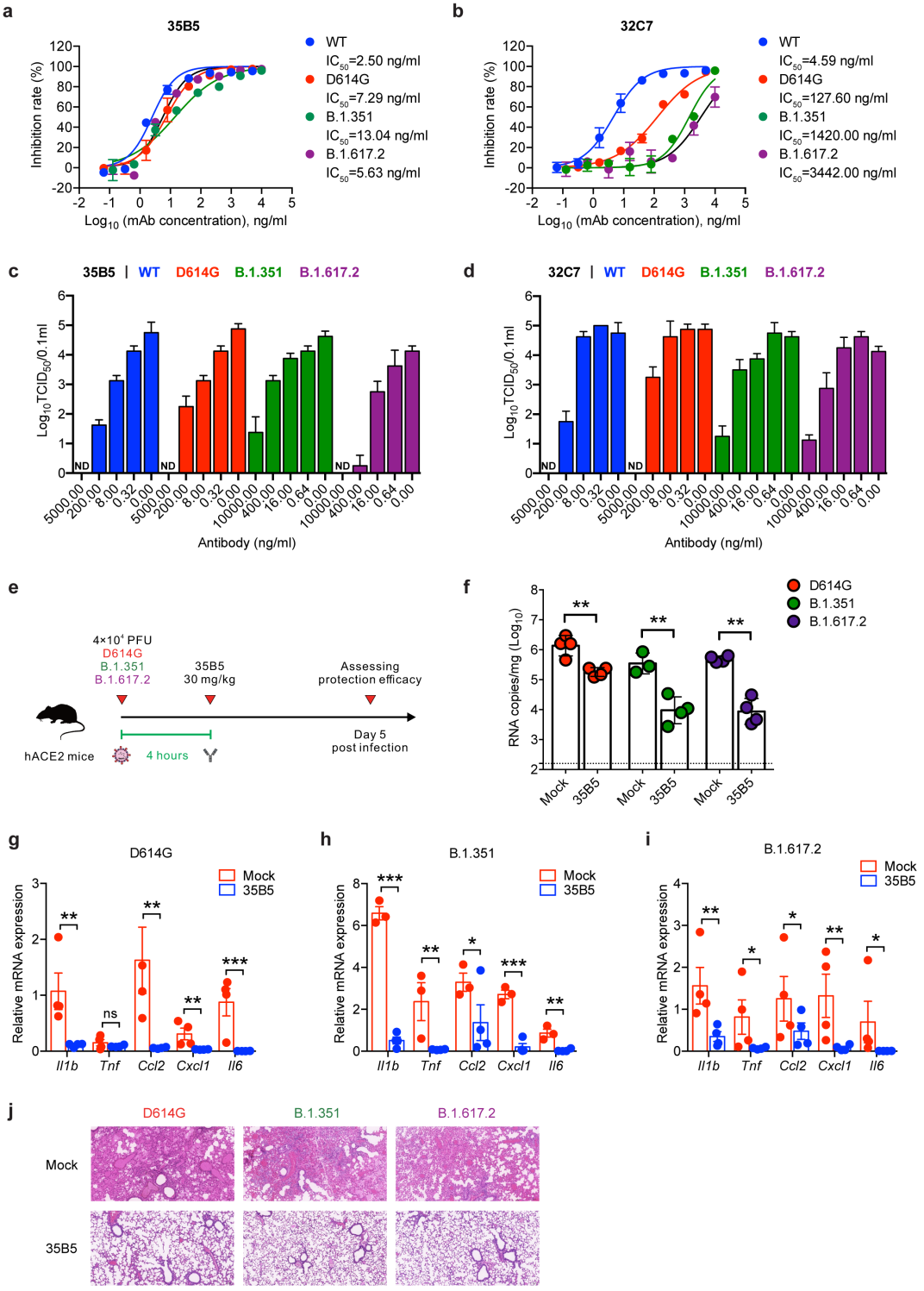


884

885

886 **Fig. 2 Neutralizing activity of 35B5 against SARS-CoV-2 VOCs**. **a, b** Neutralizing
887 activity of 35B5 (**a**) and 32C7 (**b**) against authentic SARS-CoV-2 viruses, including
888 WT strain, D614G variant, B.1.351 variant and B.1.617.2 variant. Mixture of each
889 SARS-CoV-2 strain and serially diluted 35B5 or 32C7 were added to Vero E6 cells.
890 After 48 hours, $IC_{50}$ values were calculated by fitting the viral RNA copies from
891 serially diluted mAb to a sigmoidal dose-response curve. **(c, d)** FFA analysis of 35B5
892 (**c**) and 32C7 (**d**) against WT SARS-CoV-2, D614G variant, B.1.351 variant and
893 B.1.617.2 variant. Virus cultures were serially diluted and added to Vero E6 cells.
894 After 24 hours, the foci were visualized by using HRP-conjugated polyclonal
895 antibodies targeting SARS-CoV-2 nucleocapsid protein in Vero E6 cells and counted
896 with a ELISPOT reader. **e** Schematic diagram of 35B5 treatment *in vivo*. Four hours
897 after infection with $4\times10^4$ PFU SARS-CoV-2 D614G or B.1.351 or B.1.617.2, the
898 hACE2 mice received a single dose of 35B5 with 30 mg/kg or no mAb treatment
899 (mock). At day 5 post infection, lung tissues were collected for viral burden
900 assessment. **f** Viral titers in the lungs were measured by qRT-PCR and presented as
901 RNA copies per gram of lung tissue. **g to i** Gene expressions of cytokines and
902 chemokines in the lungs were determined by qPT-PCR. **j** Histopathological analysis
903 of lung tissues. ND, not detected. Data are representative of two independent
904 experiments. Error bars in **a-d**, **f-i** indicate SD.
905

906 **Figure 3**

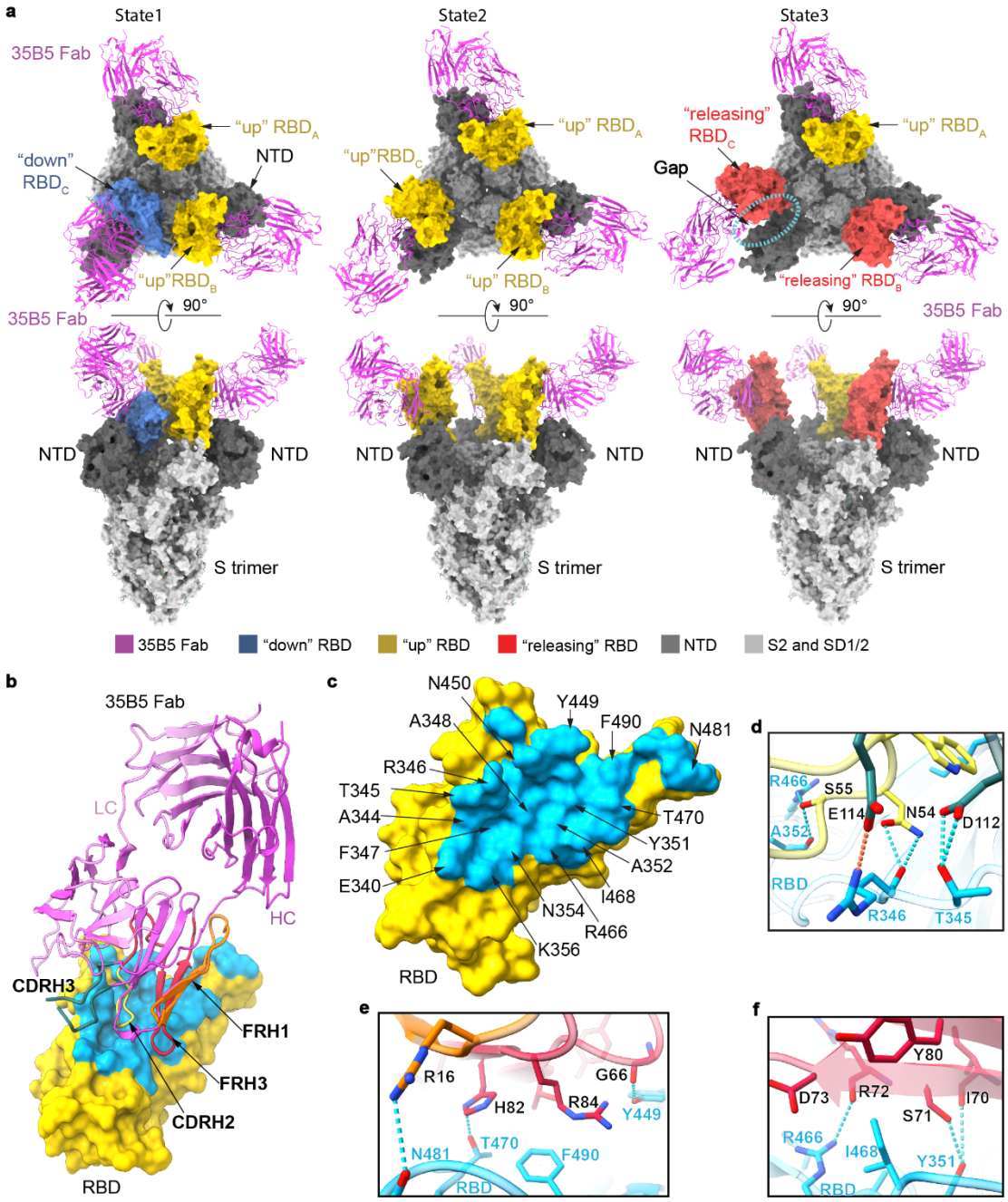


907
908

909 **Fig. 3 Cryo-EM structures of the spike protein S-6P complexed with 35B5 Fab. a**
910 The structures of the S-6P-35B5 Fab complex in three states. The S trimer is
911 represented as surface. 35B5 Fab is shown in cartoon and colored in purple. The
912 "down", "up" and "releasing" RBD domains are colored in blue, yellow and red,
913 respectively. The NTD domain of the S trimer is colored in deep grey. The SD1, SD2
914 and S2 domains are colored in light grey. The gap caused by 35B5 Fab between the
915 "releasing" RBD and NTD domains is highlighted with dashed lines. **b** Interactions of
916 35B5 Fab with "up" RBD. The interacting residues within 4 Å in RBD are colored in
917 cyan. The RBD-interacting regions CDRH2, CDRH3, FRH1 and FRH3 of 35B5 Fab
918 are colored in yellow, blue, orange and red, respectively. **c**, The 35B5 epitope on RBD.
919 The epitope residues are labeled as indicated. **d-f** Detailed interactions of the CDR (**d**)
920 and FR regions (**e** and **f**) of 35B5 Fab with RBD. Hydrogen-bond and salt-bridge
921 interactions are shown as blue and orange dashed lines, respectively.
922

923 **Figure 4**

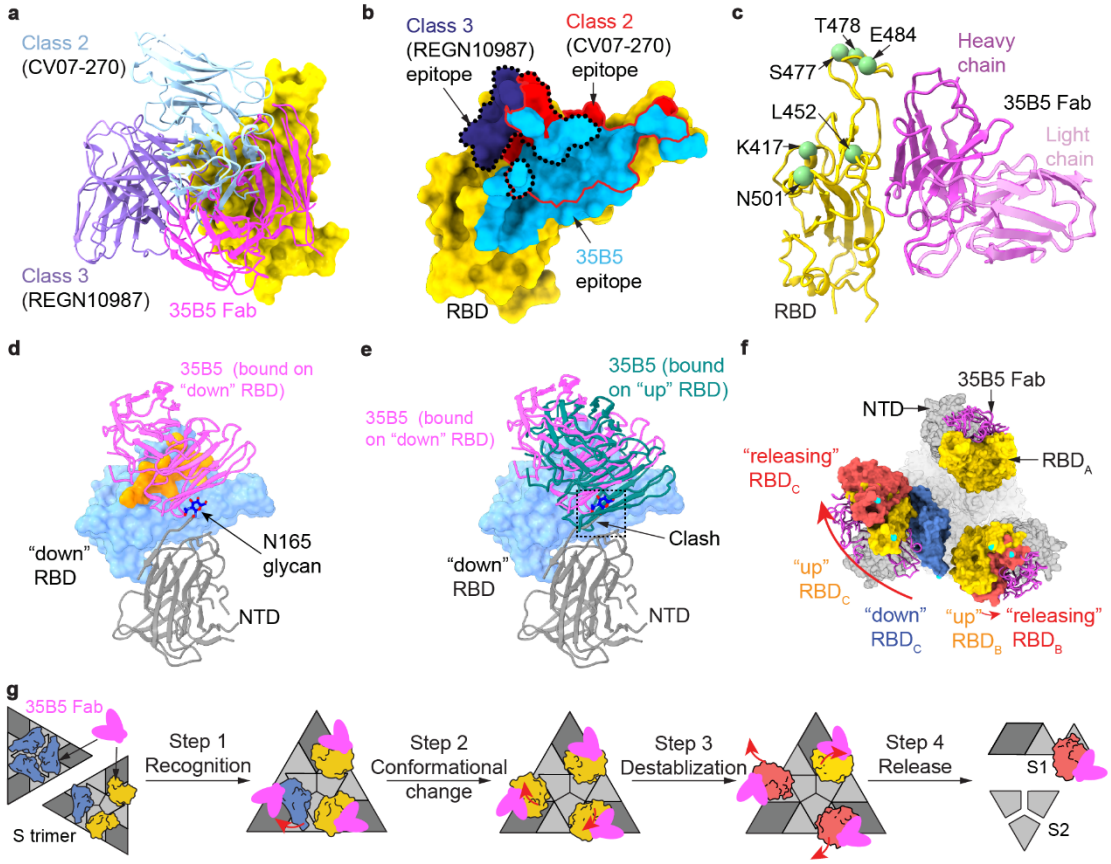


924
925

926 **Fig. 4 Structural basis and neutralizing mechanism for the broad neutralizing**
927 **activities of 35B5 to the SARS-CoV-2 variants. a** Structural comparisons of the
928 35B5 Fab-"up" RBD interactions with those of the previously identified Class 2 and 3
929 neutralizing antibodies. 35B5 Fab and the Fab regions of the representative antibodies
930 CV07-270 and REGN10987 from Class 2 and 3, respectively, are illustrated in
931 cartoon and colored as indicated. RBD is represented as surface in yellow. **b**
932 Comparison of the epitope of 35B5 with those of the representative neutralizing
933 antibodies of Class 2 and 3 on RBD. The 35B5 epitope is colored in cyan. The
934 epitopes of CV07-270 (Class 2) and REGN10987 (Class 3) are labeled using red and
935 black lines, respectively. **c** Mapping of the frequently mutated residues of the spike
936 protein in the recent SARS-CoV-2 variant in the 35B5 Fab-RBD structure. RBD and
937 35B5 Fab are shown in cartoon and colored in yellow and purple, respectively. The
938 frequently mutated residues in RBD in the recent SARS-CoV-2 variant are
939 highlighted with green spheres. **d** Interactions of 35B5 Fab with the "down" RBD.
940 35B5 Fab, the "down" RBD and NTD domains are colored in purple, cyan and grey,
941 respectively. The 35B5 Fab-interacting region on RBD is highlighted in orange. **e**
942 Structural clashes between 35B5 Fab and the NTD domain upon structural
943 superimposition of the "up" RBD-35B5 Fab model with the "down" RBD-35B5 Fab
944 region in the state 1 S-6P-35B5 Fab complex. The structural clashes are highlighted
945 with dashed lines. **f** Conformational changes of the RBD domains upon 35B5 Fab
946 binding. The S-6P-35B5 Fab complex structures of three states were superimposed.
947 35B5 Fabs are shown in cartoon in purple. The "down", "up", and "releasing" RBD
948 domains are colored in blue, yellow and red, respectively. The conformational
949 changes of RBDs are indicated with arrows. **g** Schematic diagram of the neutralizing
950 mechanism of 35B5 against SARS-CoV-2. The "down" and "up" RBDs in the
951 tight-closed or loose-closed S trimers are colored in blue and yellow, respectively.
952 The conformation changes and transmission of RBDs from the "down" to "up",
953 finally to "releasing" states are shown as red arrows.

954 **Figure 5**

a

| SARS-CoV-2 variants | Mutations in RBD |
|---|---|
| B.1.1.7 \| Alpha | N501Y |
| B.1.351 \| Beta | K417N, E484K, N501Y |
| P1 \| Gamma | K417T, E484K, N501Y |
| B.1.617.2 \| Delta | L452R, T478K |
| B.1.525 \| Eta | E484K |
| B.1.526 \| Iota | E484K |
| B.1.617.1 \| Kappa | L452R, E484Q |
| C.37 \| Lambda | L452Q, F490S |
| B.1.620 | S477N, E484K |
| P.3 \| Theta | E484K, N501Y |
| P.2 \| Zeta | E484K |
| B.1.427/B.1.429 \| Theta | L452R |

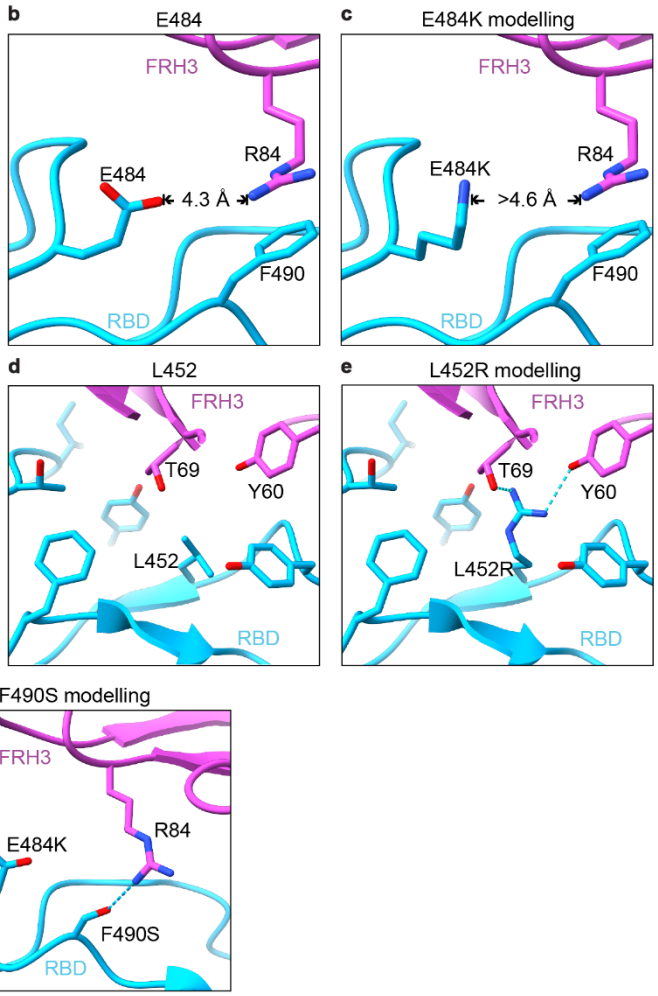


955

956

957 **Fig. 5 Interactions of 35B5 Fab with RBD. a** Mutations in the RBD of reported
958 SARS-CoV-2 variants of concern or interest. **b-g** The residues E484 (**b**) and L452 (**d**)
959 are not involved in the interactions of RBD with 35B5 Fab. E484 is more than 4.2 Å
960 away from 35B5 R84, which forms cation-π interaction with RBD F490. The E484K
961 mutation in RBD does not interact with 35B5 R84 through molecular modelling (**c**).
962 The L452Q modelling suggests none interactions formed at this site with 35B5 (**f**). In
963 structural modeling, the L452R mutation (**e**) and F490S mutation (**g**) in RBD
964 generates potential additional interactions with 35B5 Fab. Potential hydrogen bonds
965 are shown as dashed lines.

# Supplementary Figure 1

**a**

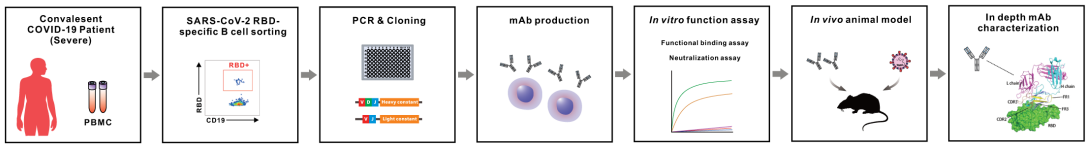


**b**

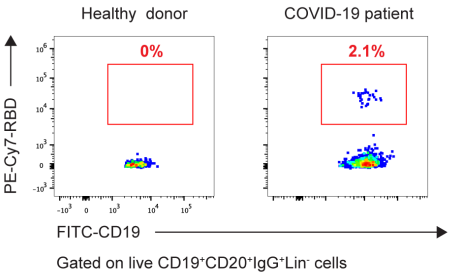


**c**

CDR3 sequence of 35B5 mAb heavy chain

A K A V E M V R G L M G L G A D P E Y G M D V

CDR3 sequence of 35B5 mAb light chain

M Q A L Q T P F T

**d**

CDR3 sequence of 32C7 mAb heavy chain

A R D T E D C S S T T C Y V D Y

CDR3 sequence of 32C7 mAb light chain

H Q Y Y S T P F T

**e**

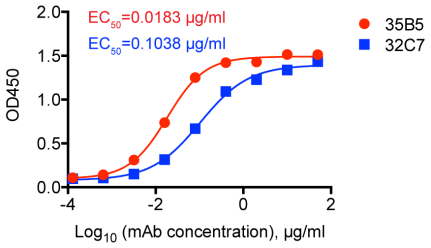

**Supplementary Figure 1. Isolation of potent SARS-CoV-2 neutralizing mAbs from COVID-19 convalescent patients. a** Isolation strategy of SARS-CoV-2 neutralizing mAbs. **b** Flow cytometry analysis of SARS-CoV-2 RBD-specific B cells from the PBMC of healthy donors and COVID-19 convalescent patients. The numbers adjacent to the outlined area indicate the proportions of SARS-CoV-2 RBD-specific B cells in $CD19^{+}CD20^{+}IgG^{+}$ B cells. **c, d** The CDR3 sequences of mAb 35B5 (**c**) and mAb 32C7 (**d**). **e** ELISA analysis of mAb 35B5 (red) or mAb 32C7 (blue) binding to SARS-CoV-2 RBD protein. $EC_{50}$, concentration for 50% of maximal effect.

**Supplementary Figure 2**

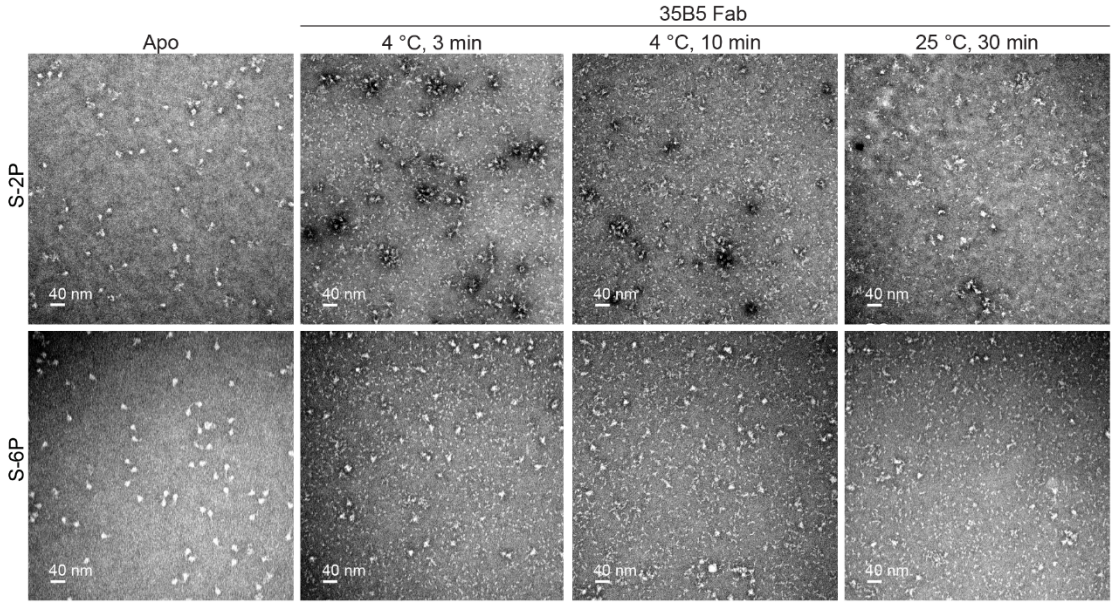

**Supplementary Fig. 2 Representative negative-staining EM micrographs of the S-2P and S-6P trimers after the treatment of 35B5 Fab.** The S-2P and S-6P trimeric proteins were treated with or without 35B5 Fab for indicated time at 4$^{o}$C or 25$^{o}$C before negative staining analysis. Scale bar, 40 nm.

# Supplementary Figure 3

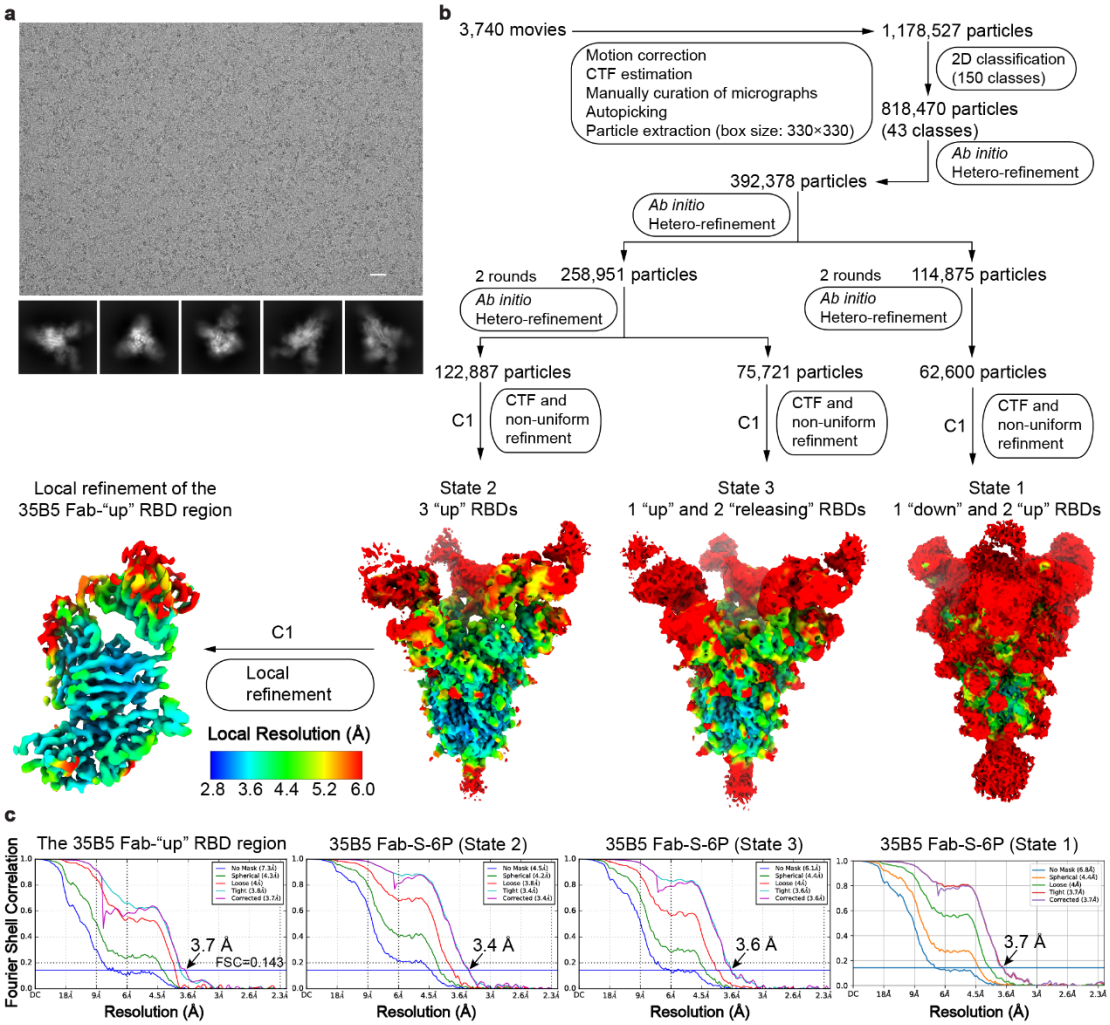

**Supplementary Fig. 3 Cryo-EM data processing and validation of the S-6P-35B5 Fab complex. a** Representative cryo-electron micrograph (upper) and 2D class averages (lower) of the S-6P-35B5 Fab complex. Scale bar, 25 nm. **b** Cryo-EM data processing flow-chart of the S-6P-35B5 Fab complex. Three states of the S-6P-35B5 Fab complex were obtained in data collection. Local refinement of the 35B5Fab-"up" RBD region was carried out using C1 symmetry (left). All density maps were prepared using ChimeraX. The map resolution is color coded for different regions. The resolution goes from 2.8 to 6.0 Å. **c** The Fourier shell correlation (FSC) curves for the reconstructions in **b**. The resolution estimations of cryo-EM density maps were based on the corrected FSC curves at the gold standard FSC=0.143 criterion.

**Supplementary Figure 4**

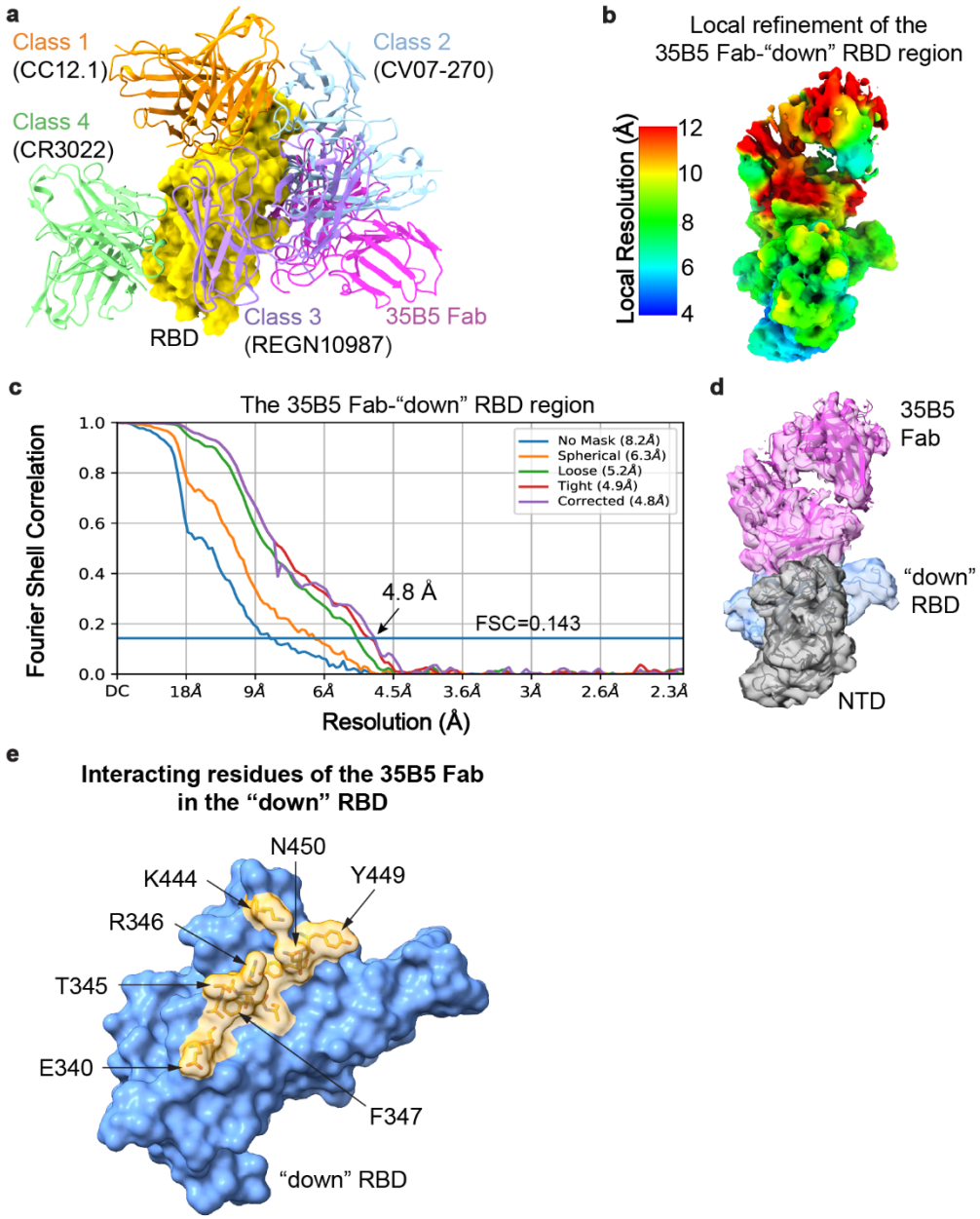

**Supplementary Fig. 4 Comparison of 35B5 with other mAbs and the local refinement of 35B5 Fab-"down" RBD region. a** Structural comparisons of the 35B5 Fab-"up" RBD interactions with those of the previously identified four classes of neutralizing antibodies. 35B5 Fab and the Fab regions of the representative antibodies CC12.1, CV07-270, REGN10987 and CR3022 from Class 1-4, respectively, are illustrated in cartoon and colored as indicated. RBD is represented as surface in yellow. **b** Local refinement of the region of 35B5 Fab with the "down" RBD and NTD domains in the State 1 S-6P-35B5 Fab complex. The density map was prepared using ChimeraX. The map resolution is color coded for different regions. The resolution goes from 4.0 Å to 12 Å. **c** The Fourier shell correlation (FSC) curve for the reconstructions in **b**. The resolution estimation (4.8 Å) of cryo-EM density maps were based on the corrected FSC curves at the gold standard FSC=0.143 criterion. **d** Structural modeling of 35B5 Fab with the "down" RBD and NTD domains in the density map obtained from the local refinement in **b**. 35B5 Fab, RBD and NTD are colored in purple, blue and grey respectively. **e** The 35B5-interacting residues of the "down" RBD. The 35B5-interacting residues of the "down" RBD (within 4 Å to 35B5 Fab) are colored in yellow.

# Supplementary Figure 5

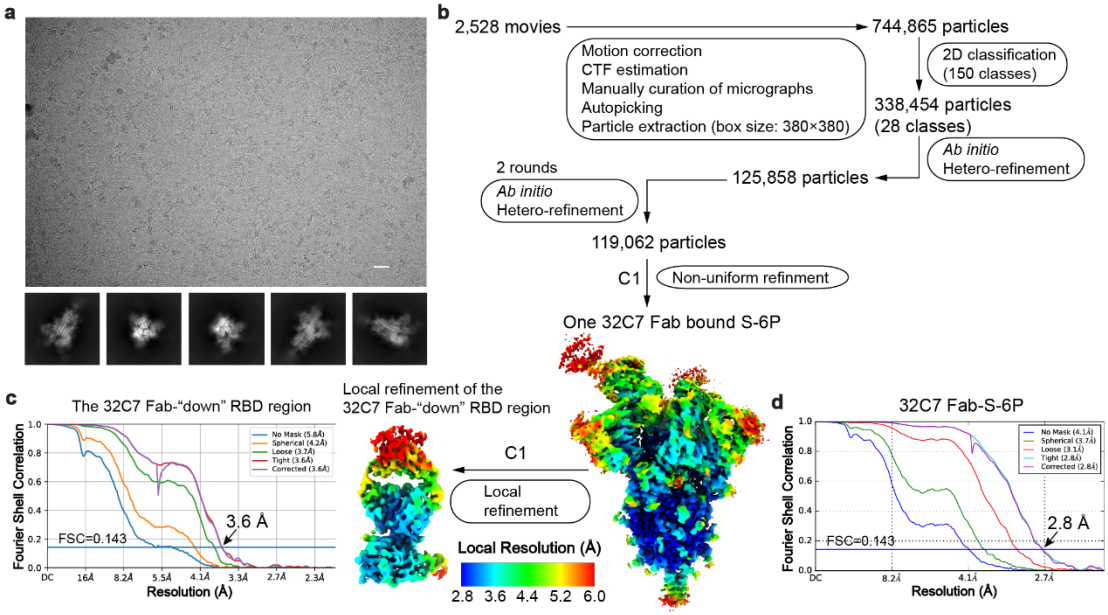

**Supplementary Fig. 5 Cryo-EM data processing and validation of the S-6P-32C7 Fab complex. a** Representative electron micrograph (upper) and 2D class averages (lower) of the SARS-CoV-2 S-6P- 32C7 Fab complex. Scale bar, 25 nm. **b** The cryo-EM data processing flow chart of the S-6P-32C7 Fab complex. Only one 32C7 Fab is bound to a "down" RBD of the S-6P trimer. Local refinement of 32C7 Fab with the "down" RBD generated a map at the resolution of ~ 3.6 Å. The density map was prepared using ChimeraX. The map resolution is color coded for different regions. The resolution goes from 2.8 Å to 6.0 Å. **c**, **d** The FSC curves for the reconstructions of the 32C7 Fab-RBD region (**c**) and the S-6P-32C7 Fab complex (**d**) in **b**. The resolution estimations of cryo-EM density maps were based on the corrected FSC curves at the gold standard FSC=0.143 criterion.

## Supplementary Figure 6

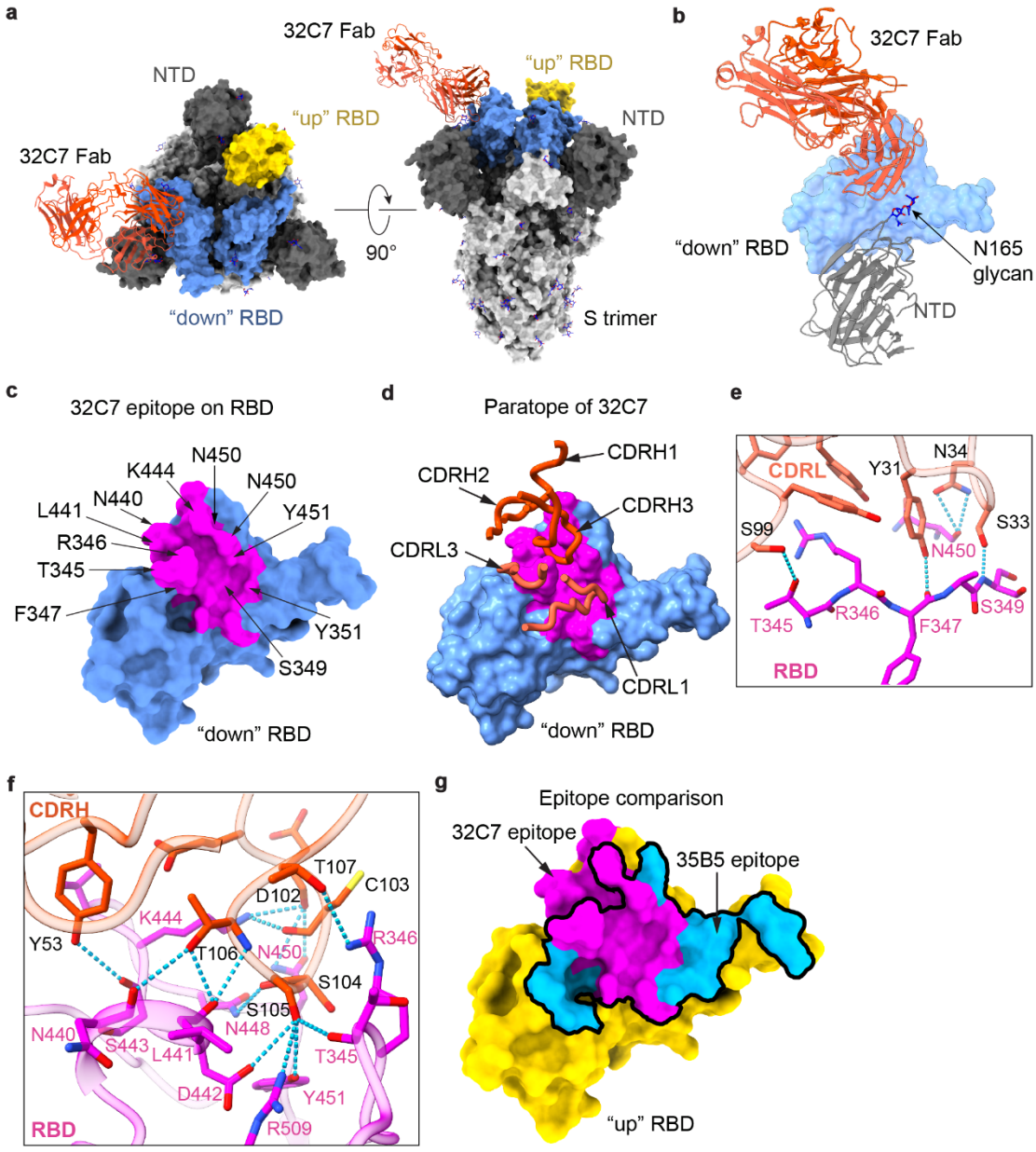

**Supplementary Fig. 6 Cryo-EM structure of the S-6P-32C7 Fab complex. a** The 2.8-Å cryo-EM structure of the S-6P-32C7 Fab complex. The S-6P trimer is represented as surface. 32C7 Fab is shown in cartoon in red. The "down" and "up" RBDs are colored in blue and yellow, respectively. **b** Structural superposition of the 32C7 Fab-RBD model and the tight-closed S trimer (PDBID: 6ZB5). In the structural superimposition, 32C7 Fab does not form structural clashes with the NTD domain of the tight-closed S trimer. RBD is shown as surface in blue. The NTD domain of the S trimer is shown in cartoon in grey. **c** The 32C7 epitope on RBD. The epitope residues are labeled as indicated. **d** The RBD-interacting regions in 32C7 Fab. The CDRH1, CDRH2, CDRH3, CDRL1 and CDRL3 are shown in ribbon. **e**, **f** Detailed interactions of the light chain CDRs (**e**) and heavy chain CDRs (**f**) of 32C7 Fab with RBD. Hydrogen-bond interactions are shown as dashed lines. **g** Comparison of the epitopes for 32C7 and 35B5 on the surface of RBD. The epitopes for 32C7 and 35B5 (black contour) are colored in purple and blue, respectively.

## Supplementary Figure 7

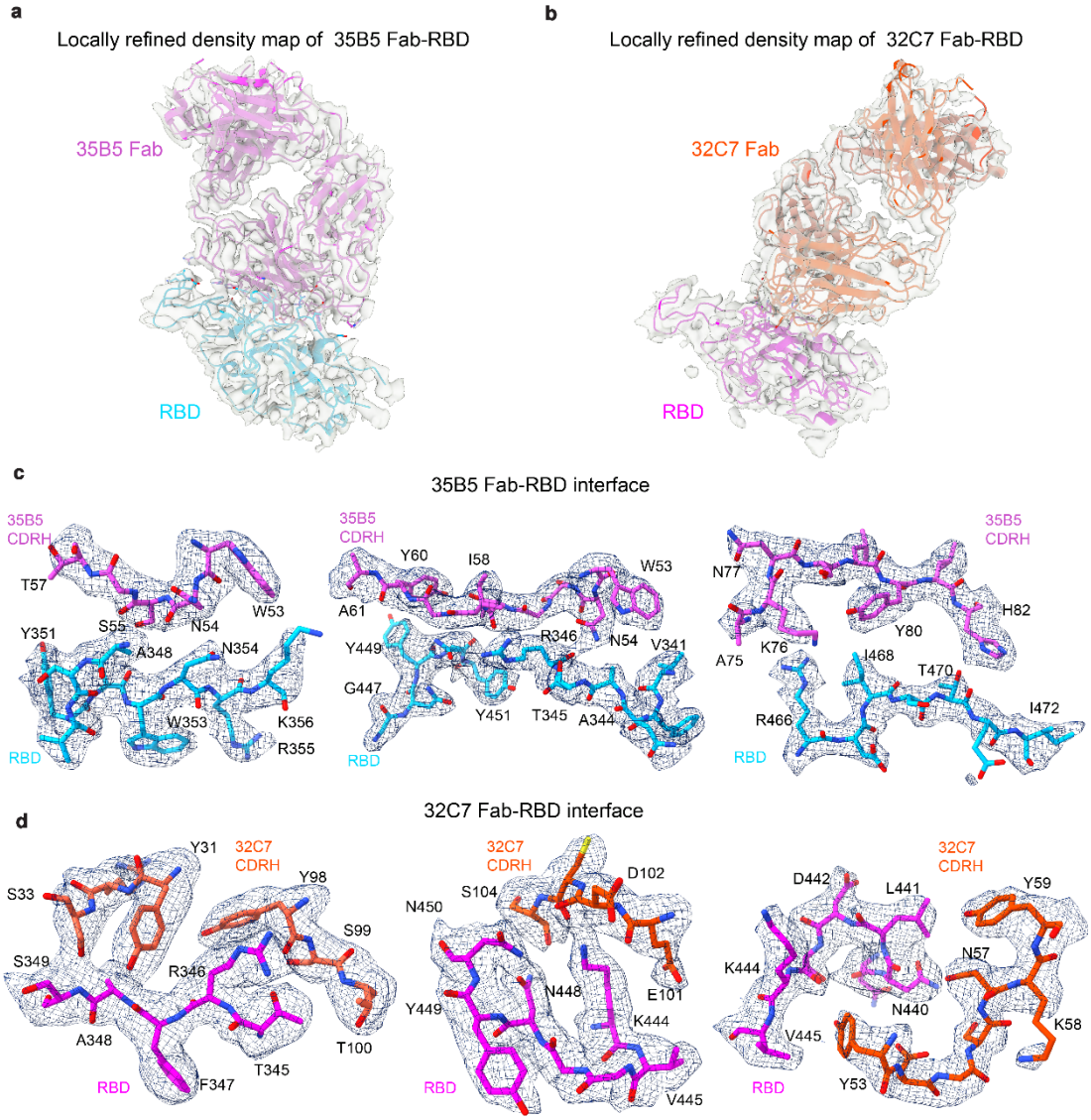


**Supplementary Fig. 7 Density maps of 35B5 Fab-RBD and 32C7 Fab-RBD interfaces after local refinement. a** Locally refined density map (transparent gray) of the 35B5 Fab-"up" RBD region in the State 2 S-6P-35B5 Fab complex. **b** Locally refined density map of the 32C7 Fab-RBD region in the S-6P-32C7 Fab complex. **c** Representative density maps of interaction regions at the 35B5 Fab-RBD interface. **d** Representative density maps of interaction regions at 32C7 Fab-RBD interface. The interacting residues of RBD and Fabs are shown as stick.

## Supplementary Table 1. Cryo-EM data collection and refinement statistics.

| | 35B5 Fab-S-6P (state 1) | 35B5 Fab-S-6P (state 1, local refinement) | 35B5 Fab-S-6P (state 2) | 35B5 Fab-S-6P (state 2, local refinement) | 35B5 Fab-S-6P (state 3) | 32C7 Fab-S-6P | 32C7 Fab-S-6P (local refinement) |
|---|---|---|---|---|---|---|---|
| **PDB code** | **7E9N** | **7F46** | **7E9O** | **7E9P** | **7E9Q** | **7ENF** | **7ENG** |
| **EMDB code** | **EMD-31033** | **EMD-31444** | **EMD-31034** | **EMD-31035** | **EMD-31036** | **EMD-31209** | **EMD-31210** |
| **Data collection and processing** | | | | | | | |
| Voltage (kV) | 300 | 300 | 300 | 300 | 300 | 300 | 300 |
| Magnification | 81,000 | 81,000 | 81,000 | 81,000 | 81,000 | 81,000 | 81,000 |
| Pixel size (Å/pix) | 0.5475 | 0.5475 | 0.5475 | 0.5475 | 0.5475 | 0.53865 | 0.53865 |
| Frames per exposure | 32 | 32 | 32 | 32 | 32 | 32 | 32 |
| Exposure ($e^-$/Å$^2$) | 50 | 50 | 50 | 50 | 50 | 50 | 50 |
| Defocus range (μm) | 1.2 to 1.3 | 1.2 to 1.3 | 1.2 to 1.3 | 1.2 to 1.3 | 1.2 to 1.3 | 1.4 to 1.8 | 1.4 to 1.8 |
| Final particle images (no.) | 62,600 | 62,600 | 122,887 | 122,886 | 75,721 | 119,062 | 119,062 |
| Symmetry imposed | C1 | C1 | C1 | C1 | C1 | C1 | C1 |
| Map resolution (Å, 0.143 FSC threshold) | 3.7 | 4.8 | 3.4 | 3.7 | 3.6 | 2.8 | 3.6 |
| **Refinement** | | | | | | | |
| Map resolution (Å, 0.5 FSC threshold) | 3.9 | 8.6 | 3.7 | 3.9 | 3.8 | 3.0 | 3.7 |
| Map sharpening *B* factor (Å$^2$) | 81.9 | 115.6 | 90.4 | 86.3 | 82.5 | 75.8 | 110.2 |
| Model composition | | | | | | | |
| Protein residues | 4,313 | 842 | 4338 | 639 | 4,338 | 3,390 | 640 |
| Ligands | 27 | 2 | 27 | 1 | 27 | 53 | 2 |
| R.m.s. deviations | | | | | | | |
| Bond length (Å) | 0.008 | 0.005 | 0.004 | 0.005 | 0.005 | 0.005 | 0.006 |
| Bond angles (º) | 0.870 | 0.757 | 0.768 | 0.849 | 0.887 | 0.835 | 0.802 |
| Ramachandran plot | | | | | | | |
| Favored (%) | 91.61 | 91.12 | 95.12 | 92.53 | 93.60 | 94.70 | 92.59 |
| Allowed (%) | 8.39 | 8.88 | 4.88 | 7.47 | 6.40 | 5.30 | 7.41 |
| Outliers (%) | 0 | 0 | 0 | 0 | 0 | 0 | 0 |
| Validation | | | | | | | |
| Poor rotamers (%) | 0.11 | 0 | 0.24 | 0 | 0.32 | 0.56 | 0.36 |
| Clash score | 12.95 | 18.16 | 10.62 | 11.97 | 14.62 | 10.14 | 14.32 |
| MolProbity score | 2.12 | 2.27 | 1.88 | 2.06 | 2.09 | 1.89 | 2.13 |